Universidad Nacional Autónoma de México

Instituto de Radioastronomía y Astrofísica

PhD. in Science
(Astrophysics)

Advance of doctoral project

Study of the existence of Active Galactic Nuclei of the evolution and disappearance of the torus through X-rays

PRESENTS:

Natalia Osorio Clavijo

ADVISOR:

Dra. Omaira González Martín

June 2021

1 Introduction

It has been widely accepted that all galaxies with developed bulges, host a super massive black hole (SMBH), which in some cases is being fed by an accretion disk, causing the liberation of energy of orders up to bolometric luminosities L $\sim 10^{44}$ erg s^{-1}. The nuclei of galaxies with such phenomenon are known as active galactic nuclei (AGN), and can emit through all the electromagnetic spectrum. According to the standard model (Urry and Padovani, 1995) AGN are composed by several regions apart from the accretion disk. Such regions are made up from clouds of dust and gas, although their formation and evolution are still under debate. Among the components, we find **the SMBH**, whose mass can be of the order of $\sim 10^6 - 10^{10}$ M$_\odot$, **the accretion disk**, which is responsible for the accretion onto the SMBH and most of the energy released. The temperature of this structure places the peak of emission at optical/UV wavelengths. **The broad line region (BLR)** is placed beyond the accretion disk and is formed by clouds of gas, with speeds of several thousands of km/s (Davidson and Netzer, 1979), producing the broadening of lines emitted in the optical and infrarred range (e.g., Hα, Hβ, the Paschen series, etc.) This region is surrounded by **the torus**, a region composed by dust that is heated by the accretion disk up to a few 1000 of K, placing the peak of its emission at infrared wavelengths. Although classically thought of as a doughnut, the geometry of this structure has been widely debated and its evolution throughout different types of AGN is still matter of study. In fact, different models with different geometries and distributions have been developed in order to understand the true nature (see, Fritz et al., 2006; Nenkova et al., 2008a; Hönig and Kishimoto, 2010, 2017, etc). This region is thought to be responsible for the reflection feature at X-rays due to the neutral gas located in the inner parts of it. **The narrow line region (NLR)** is the most extended region in AGN, and the only one that has been resolved through optical telescopes. This region is mostly composed by ionized gas and the clouds in it are moving at velocities of hundreds of km/s (Bennert, 2005). In some cases, a **relativistic jet** is also visible, emitting mostly at radio-frequencies.

Classifying an object as an AGN has long been matter of debate due to the difficulties in different wavelengths. For instance, through optical wavelengths, the fact that many of them are buried behind large amounts of material and that the host galaxy may even dilute the AGN emission (Davies et al., 2016), may be preventing us from seeing the less-luminous and/or obscured AGN in these range. In the optical, AGNs can be classified as Type-I if their spectra show both broad and narrow lines, whereas Type-II AGN present only narrow line (since the BLR is hidden). With this classification, the Unified Model of AGN (UM, see below) was proposed to explain the different types of AGN as seen from the optical wavelengths. However AGN are classified in different wavelengths, as these trace different physical mechanisms and regions. For instance, through radio, AGN can be distinguished as radio quiet/loud depending on their radio luminosity, thought to be linked to the jet emission. Moreover, these jets can be distinguished between FR-I/FR-II depending on whether the peak in luminosity occurs on the core or on the lobes of the jet (Fanaroff and Riley, 1974). Also, through X-rays they can also be classified as Compton-thin/Compton-thick depending on the column density through the line-of-sight to the observer. AGN can also be classified depending on the accretion state, closely related to the bolometric luminosity. Thus, we find from quasars, the most luminous sources, to Seyferts, which have average luminosities, and even the so-called Low-Luminosity AGN (LLAGN, Heckman, 1980) which reside in the lowest tail of the luminosity function for AGN. These objects are classified as those with $L_{\rm bol} < 10^{42}$ erg s^{-1}, and are thought to be the link between normal and active galaxies (Márquez et al., 2017). These objects have a different spectral energy distribution (SED) compared to more luminous AGN (e.g., Seyferts, Nemmen, 2013). Additionally, these objects are the most common type of AGN in the nearby Universe (Ho, 2008). In order to explain their low accretion and luminosity, it has been proposed for the accretion mechanism to differ from the standard accretion disk (Shakura and Sunyaev, 1973), in what is known as the Advection Dominated Accretion Flow (ADAF, Narayan and Yi, 1994). Another scenario is that these objects are highly obscured, thus the population of these objects might be underestimated (González-Martín et al., 2009).

The Unified Model (UM, Antonucci, 1993; Urry and Padovani, 1995, see Fig. 1) of AGN proposes that all the aforementioned regions are present in every AGN but its classification depends on a few observational parameters, being one of the most important the viewing angle toward the observer. Thus, if the observer is seeing the torus along the line-of-sight (LOS), the BLR may be hidden behind it and thus only narrow lines are present in the optical spectrum. Therefore, the cornerstone of the UM is the existence of the torus. Under the simplest version of the UM scenario, the torus is a homogeneous doughnut-like structure composed mainly by dust and gas. However, one of the main problems of the UM is the fact that it cannot explain all the AGN classes (for instance changing-look AGN or low-luminosity AGN). Thus, models aiming to explain the different AGN types have been extensively developed and have found that the torus may not be as homogeneous and smooth as the UM states. In particular, these models have been divided depending on the geometry, distribution and chemical composition of the dust in torus (e.g., Fritz et al., 2006; Nandra et al., 2007; Nenkova et al., 2008b; Hönig and Kishimoto, 2010). Another problem of the Unified Model, is that it does not take into account the possible connection between the AGN and the host galaxy. Indeed, Krongold et al. (2002) found hints on the evolution of the AGN, where those subject to larger amounts of obscuring material in the LOS are mostly found for galaxies with large star formation rates and signs of recent merger events. Indeed, they find most AGN in their sample to be hosted by galaxies with significant star formation and immersed in interacting systems. Therefore, it is required more information to determine which aspects of the UM should be modified or if on the contrary, the entire scenario is still valid.

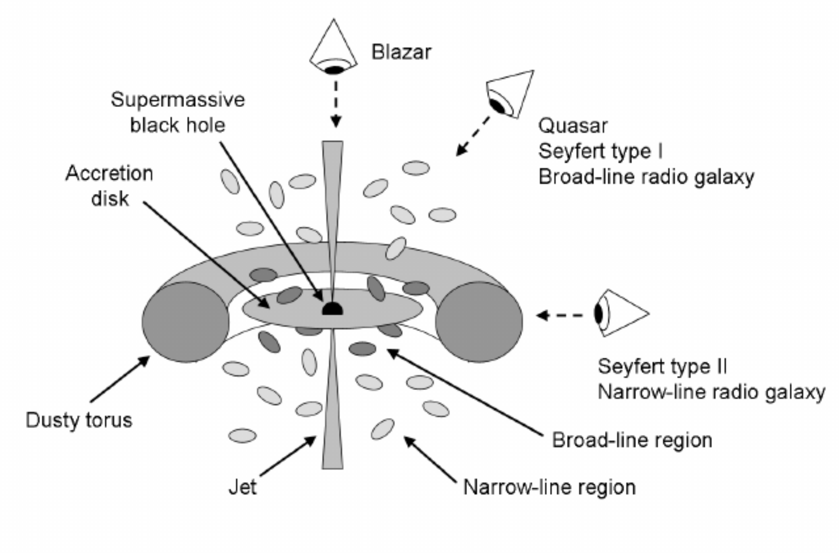

Figure 1: Unified Model of AGN. Taken from Zackrisson (2005).

1.1 X-ray spectra of AGN

The AGN emit in all the electromagnetic spectrum, and different wavelengths give us hints on the diverse physical mechanisms occurring in them. Our work is focused on the X-ray band. These energies are important to determine whether a galaxy hosts an AGN, and understand its circumnuclear emission, as well as to understand the emission mechanism of these objects with the spectroscopic analysis. Part of the X-ray AGN emission comes from the reprocessing of the disk emission in what is known as the X-ray corona. This region is thought to be located above the accretion disk and, through inverse Compton-scattering, it reprocesses the UV photons and re-emits them at X-rays. This emission is known as primary continuum and is usually partially-covered by clouds in the LOS toward the observer. By modelling this emission, we can study the obscuration in the LOS with the use of spectroscopic fitting to physical models, which also account for different obscuring scenarios (i.e., uniform or partial-covering). Additionally, most of the emission above 10 keV is associated with the reflection occurring either in the accretion disk or in regions further away from it such as the BLR and/or the torus (see Fig. 2, right). Note that we aim to study the reflection component, which is characterized by two main features: the Fe XXV (FeKα) line peaking at 6.4 keV and the Compton hump. The latter is dominant for highly obscuring material, even suppressing the intrinsic emission for Compton-thick objects (i.e., objects for which the column density $N_H > 10^{24.5}$ cm^{-2}). Note that this work assumes that most of the reflection component is originated in the distant and neutral torus, which has been demonstrated to be the case for most type-2 intermediate and low luminosity AGN Ricci et al. (2011), as those studied here. Indeed, the reflection originated in ionized material (such as that from the BLR or the disk) shows characteristic emission line features in the soft X-rays (Ezhikode et al., 2020), which has not been detected in our sources (e.g., González-Martín et al., 2009; Kawamuro et al., 2016)

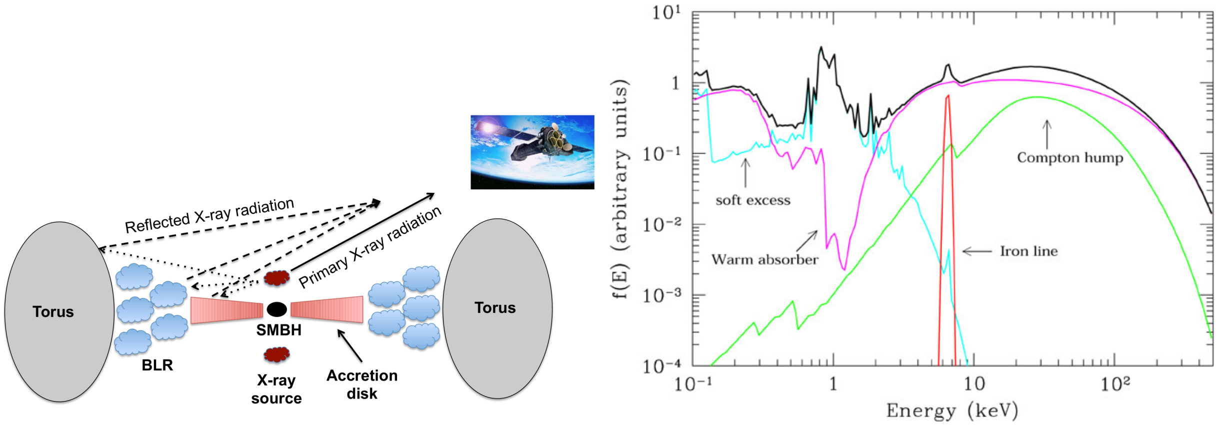

Figure 2: Left: AGN components as seen from the X-ray point of view. Right: AGN X-ray spectra. Each component is represented in the colors as follows: Magenta represents the absorbed intrinsic continuum, green is the Compton-hump, which is a reflection feature, as well as the FeKα line (in red). The soft excess (cyan) which may be related to host galaxy emission or scattered emission from the corona. Taken from Ricci 2011. PhD thesis.

2 State of the art and goals

This thesis is divided into two main goals: (1) to find possible connections between the AGN and the plausible torus disappearance, and (2) to find and characterize AGN candidates from the CALIFA sample.

2.1 AGN torus evolution and disappearance

From a theoretical point of view, it has been proposed that the AGN torus can disappear for low luminosities (Elitzur and Shlosman, 2006). This can be explained if both the BLR and the torus are structures formed from an outflow coming off the accretion disk, and for which the radiation field cannot counteract the gravitational field from the SMBH. Thus, the torus should disappear for luminosities $L_{bol} < 10^{42}$ erg s^{-1}. However, in more recent works, it has been proposed that the torus can disappear even for bright sources, depending on the different wind parameters, such as density and efficiency at expelling material, but also the black hole mass, radial density of the wind, etc., although it can be characterized with the black hole mass ($L_{lim} = 4.7 \times 10^{39} M_{BH}^{2/3}$ erg s^{-1}, Elitzur and Ho, 2009). We aim to understand the conditions behind this evolution, and therefore we choose a sample with a wide range of bolometric luminosities ($\log(L_{bol}) = [42-45]$) classified as both Type-I and Type-II, to see if this evolution aligns with the UM.

We to investigate if the reflection component is intrinsically different for LLAGN. Ricci et al. (2011) showed that reflection at X-rays is intrinsically larger in Type-II than in Type-I. González-Martín et al. (2015), in an analysis performed for LLAGN with mid-Infrared (MIR) observations, found evidence for the torus disappearance at these low luminosities, which was later confirmed by González-Martín et al. (2017). In order to compare and support or deny these results found at MIR, we use X-ray observations. This will allow us to compare the reflection component detected at X-rays with the torus emission detected at MIR and see if they are both produced in the same region. In particular, Esparza-Arredondo et al. (2019) found, through a simultaneous fit between X-rays and MIR, that both components come from the same region for IC 5063, a Type-II object. Nonetheless, it is necessary to see if this is the average behaviour for type-II AGN, which is the aim of Esparza-Arrendondo et. al (2021 A&A accepted).

Finally, we also aim to understand if the fraction of obscured sources depends on the Eddington rate or luminosity within LLAGN. For instance, Ricci et al. (2017) found that the peak of obscured sources occurs at at Eddington rates $\lambda_{Edd} \sim 10^{-3}$. However, they used the *Swift* satellite which does not observe lower luminosities. This work will extend the work done by Ricci et al. (2017), toward the lowest luminosities detected by the *Nuclear Spectroscopic Telescope Array (NuSTAR)*. This telescope has a large energetic range (3-79 keV) which will allow us to study the broadband spectra of different types of AGN.

2.2 AGN candidates from the CALIFA sample

Among the methods for the classification of ionization mechanisms in galaxies, we find the Baldwin, Phillips & Terlevich (BPT Baldwin et al., 1981) diagrams. These diagnostic diagrams allow to compare the different ionization mechanisms in galaxies by analyzing line ratios. The most common ratios are: [NII]/Hα vs [OIII]/Hβ, [SII]/Hα vs [OIII]/Hβ and [OI]/Hα vs [OIII]/Hβ. Kewley et al. (2001, 2006) determined limits to distinguish between starburst galaxies, low-ionization narrow line emission regions (LINERs) and AGN, while Kauffmann et al. (2003) established limits to distinguish between normal and active galaxies. We can use these diagrams to determine which ionization mechanism is the dominant, but also to see the different mechanisms present in a galaxy. Fig. 3 shows the location of different galaxies with different dominant mechanisms from the CALIFA sample (Lacerda et al., 2020). These diagrams are useful when used in luminous AGN, although they present issues for LLAGN/LINER since the star formation processes may hide the AGN within the galaxy.

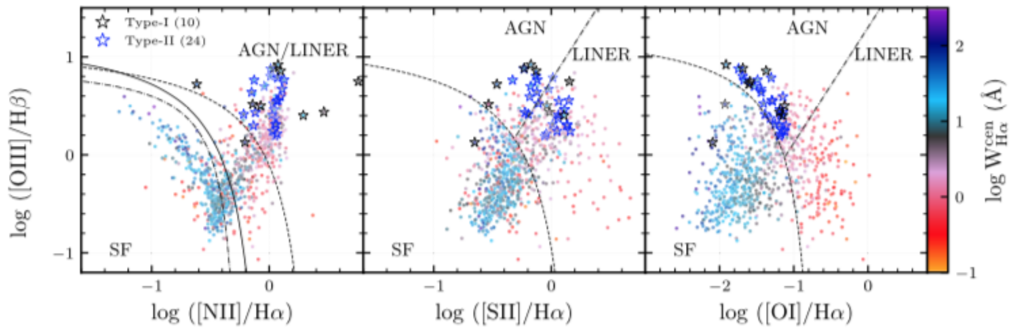

Figure 3: BPT diagnostic diagrams from Lacerda et al. (2020). The dashed lines represent the delimited zones (Kewley et al., 2001, 2006), while the solid line represents the distinction between a normal and SF galaxy, from Kauffmann et al. (2003). The stars represent the AGN candidates in their sample, clearly occupying the AGN region of the diagrams.

In a recent work by Lacerda et al. (2020), they searched AGN in the *Calar-Alto Legacy Interal Field spectroscopy Area survey* (CALIFA) sample. This sample contains 867 sources and each of the galaxies were selected such that the sources filled the Field-of-view (FOV) of the instrument. These galaxies have a range of masses log $[\mathrm{M/M_\odot}]$ $[7.6-11.9]$ and are located in the nearby Universe (z $[0.001-0.08]$). According to Lacerda et al. (2020) $\sim 4\%$ of the sample host an AGN. From the 34 AGN sources found, they classify 10 as Type-I and the remaining 24 as Type-II. Moreover, AGN feedback is assumed to be the main mechanism to quench star formation in massive galaxies (e.g., Hopkins et al., 2009). Therefore, a correct detection of the presence of an AGN in galaxies is fundamental to understand the evolution of them. In agreement with this AGN/host galaxy connection, Lacerda et al. (2020) found that their AGN hosts populate the green-valley regime (i.e., the transition zone between SF and quiescent galaxies). Moreover, they found that these AGN have well established Equivalent widths of the Hα emission line with values corresponding to those of the GV galaxies (i.e., $3\text{Å} < \mathrm{EW(H\alpha)} < 10\text{Å}$. They also found that the host galaxies are mainly classified as Sb, Sc, supporting the evolutionary model. Note that LLAGN are mostly hosted in elliptical galaxies, which may result in an underestimation of the AGN density due to the dilution from the host galaxy. Thus, the optical classification may be limited towards efficient nuclear activity. Another reason for the low density of AGN is the large obscuration along the LOS. According to the gas-to-dust ratio, the column density of neutral gas of $\sim 10^{22}\mathrm{cm^{-2}}$, produces reddening in the E(B-V) bands of over 10 magnitudes in the optical wavelengths (Kahre et al., 2018), alleviating the AGN emission at these wavelengths.

Alternatively, our approach is to classify AGN sources through the X-ray band. It has been extensively done by sky mappings (e.g., COSMOS, Hasinger et al., 2007). Indeed, the classification of AGN through the X-rays is based on the detection of a point source and on the shape of the X-ray spectrum (see Fig. 2, right) although it is also necessary to consider the hot gas from e.g., clusters. We will use X-ray observations to identify and characterize the properties of AGN in the CALIFA sample and to compare them with the AGN obtained from the classical optical diagrams. Previous attempts have used SDSS optical spectra, which limited aperture imposes a mixing of ionization conditions (Davies et al., 2016) on top of the intrinsic problems of classifying AGN in the optical regime.

2.3 Goals

2.3.1 The AGN torus evolution and disappearance

We aim to study the reflection component seen at X-rays and understand if there is an evolution of this component with the AGN luminosity. We also aim to find if there is a correlation of this component with the obscuration measured at X-rays affecting the primary continuum. The study of such component requires data above 10 keV, which is only possible with *NuSTAR* data. For this part of the project we use data from this satellite only.

2.3.2 AGN classification from the CALIFA sample

This part of the thesis is divided in two blocks. Firstly, we aim to compare the optical morphology with the X-ray extended emission by using *Chandra*. This satellite is chosen since it provides the best spatial resolution, which is necessary for our analysis. We also study the spectra from the extended emission to understand the physical processes of this emission and see if it belongs to the AGN or to the host galaxy. Additionally, we study the point-like emission and see if it is in agreement with the X-ray spectrum of an AGN.

For the second part of the project, we aim to characterize the X-ray spectrum with better spectral resolution data, accounting for the decontamination from extended emission. For this reason, we search available data in (*XMM*-Newton and *NuSTAR*) in order fully characterize the physical processes occurring in the AGN, and to understand whether they are linked to what is seen in the optical ranges.

3 Torus evolution

In this section we summarize the main results of the PhD project related to study the torus evolution. This part of the project is already finished and the paper is under referring.

We began our sample selection by searching all the available galaxies within a 10 arcmin radius for all archived pointings in the *NuSTAR* database. We obtained a total of 1313 galaxies with distances $D < 200$ Mpc, which will allow us to map the nearby Universe. We then restricted our search by excluding those galaxies not classified as AGN in neither the NED nor SIMBAD databases. We obtained a total of 463 AGN classified galaxies. We then retrieved the SMBH mass for these sources in order to estimate the Eddington rate, defined as $\lambda_{\rm Edd} = \rm L_{Edd}/L_{bol}$. We firstly looked for $\rm M_{BH}$ values calculated via reverberation mapping (e.g. Laor, 2001, 2003; Woo and Urry, 2002; Vasudevan and Fabian, 2009) and velocity dispersion otherwise (e.g. McKernan et al., 2010; van den Bosch et al., 2015; van den Bosch, 2016), by using the M-σ relation, $\rm M_{BH}$ ($\log(\rm M_{BH}/M_{\odot}) = 8.27 + 5.1\log(\sigma/200$ km s^{-1}) Ferrarese and Merritt, 2000; Gebhardt et al., 2000). As for the sources for which the $\rm M_{BH}$ value is not calculated through the methods reported above, we also searched in different BH mass catalogues reported (e.g. Khorunzhev et al., 2012; Koss et al., 2017; Bär et al., 2019). We obtained black hole mass measurements for 231 out of the 301 AGN. There sources were later fitted to a simple unabsorbed power-law to obtain the X-ray luminosity in the 2-10 keV and then the bolometric luminosity. We finally kept only those sources for which the Eddington rate is $\lambda_{\rm Edd} < 10^{-3}$. Such constraint on the Eddington rate is imposed to ensure that we study the least efficient objects with available *NuSTAR* data. We reduced the spectra by using the *NuSTARDAS* package *NuSTARDAS* v.1.4.4 and extracted a circular region maximizing the signal-to-noise ratio, by varying this region from 30 to 120 arcsec. However, we find for this radius to be on average around 60 arcsec. The table with the observational parameters of the sample can be seen in the Appendix. The *NuSTARDAS* pipeline uses the task `nuproducts` which generates the images, spectra and light curves of the observations. We also group the spectra with the condition of at least 30 bins per channel with the `grppha` task. This is done in order to use the chi-squared statistic. The source selection is done with DS9 (an example of this is shown in Fig. 4 for NGC 3079, for which the optimal radius is 30 arcsec.

For the spectral analysis, we fit the extracted spectra with four models, each one adopting a different possible scenario for the observed emission. For the first model, we assume a primary continuum partially covered by clouds along the line-of-sight, and additional ionized lines commonly found in AGN.

$$M_1 = \texttt{phabs}_{\rm Gal}((\texttt{zphabs}_{\rm intr} * \texttt{zpowerlw}) + \texttt{ct} * \texttt{zpowerlw} + \texttt{zgauss}_{\texttt{6.7 keV}} + \texttt{zgauss}_{\texttt{6.97 keV}}) \quad (1)$$

For this first model, we allow the following parameters to vary: (i) the photon index of the power-law, (ii) the column density along the LOS, (iii) the constant associated with the scattering fraction, and (iv) the

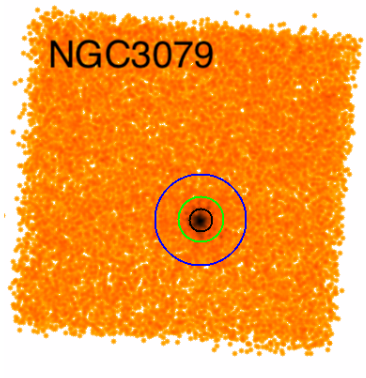

Figure 4: Source selection for NGC 3079. The black, green and blue circles correspond to apertures of 30, 60 and 120 arcsec. In this case, the optimal radius is 30 arcsec.

normalization of each component. The rest of the parameters are set to their default values: the redshift is set to its value for each source and width of the Gaussian line is set to 0.1 keV (assuming a narrow profile). Note that we also account for Galactic absorption from the HI maps (Kalberla et al., 2005) and that the normalization and photon index of both power-laws are linked to each other.

The second model is a complement of the first one, where we add a reflection component from neutral material, classically associated with the distant torus and the FeKα, which is one of the main indicators of reflection in X-rays. In the software terminology,

$$M_2 = M_1 + \texttt{phabs}_{\rm Gal}(\texttt{pexrav} + \texttt{zgauss}_{\texttt{6.4 keV}}) \quad (2)$$

For this model version, the free parameters is: (i) the normalization of `pexrav` and (ii) the normalization of the FeKα line, while the photon index is linked to that of the first model, the Energy cutoff is set to 300 keV, since we expect for this cutoff to be well above the *NuSTAR* range and the relative reflection is set to -1, which emulates the scenario of full-reflection for the `pexrav` model component. In addition, we set photon index of this component to be the same as that of the intrinsic continuum power-law, while rest of the parameters are set to their default values: the abundance is set to 1, which assumes a solar abundance of Fe and elements heavier than the He, while the cosine of the inclination angle is set to 0.45. The third model is a more complex model for the reflection, which includes the level of ionization of the medium with the addition the FeKα, FeKβ and NiKα lines, which makes of it a more realistic model.

$$M_3 = M_1 + \texttt{phabs}_{\rm Gal}(\texttt{pexmon}) \quad (3)$$

In reality, both M_2 and M_3 are equivalent, although the reflection component differs as `pexrav` does not account for the FeKα line associated with the torus. Thus, we use the M_2 model to estimate and characterize the line properties as Equivalent Width (EW) and luminosity, and trace their possible evolution with the AGN luminosity. On the other hand, we use M_3 to study the reflection as a whole.

Finally, we also include a fourth model to test the scenario in which the source is reflection dominated (i.e. a model consisting on a pure reflection component) . We use this model when the reflection component is statistically necessary in M_3.

$$M_4 = \texttt{phabs}_{\rm Gal}(\texttt{pexmon}) \quad (4)$$

Note that our baseline model has been widely used in several works aimed to find general properties of AGN and characterize the reflection component, even in Compton-thick (CT) objects (e.g., Kawamuro et al., 2016; Panagiotou and Walter, 2019, 2020; Kang et al., 2020). Thus, the baseline model used in this work will lead to robust results that can be easily compared with previous works (e.g., Kawamuro et al., 2016; Annuar et al., 2015, 2017, 2020).

Throughout all the analysis we use the chi-square statistic and the f-test to establish which among the four scenarios is the preferred one, for each of the sources. We define that one model is statistically better than another one if the f-test returns a low value[1]We keep the best-fit values for all the free parameters, while the errors are reported as follows: if the parameter is restricted above $3-\sigma$, we list the $1-\sigma$ error.

[1]see https://heasarc.gsfc.nasa.gov/xanadu/xspec/manual/node83.html.

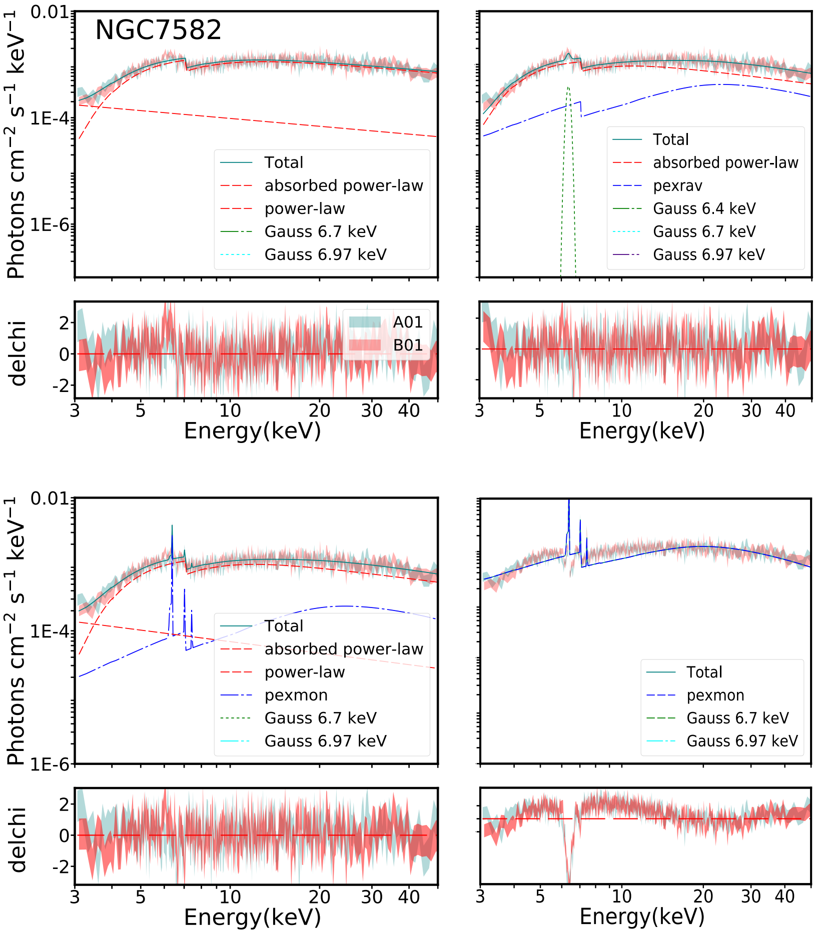

Figure 5: Spectral fits for M_1 (upper left), M_2 (upper right), M_3 (lower left) and M_4 (lower right) for NGC 7582. Each color represents each of the components as follows: teal is the total spectrum, red is the partial-covering component, blue are pexmon (left) and pexrav (right) components, while green, cyan, and purple are the extra lines in each model version.

However, if it is not the case, then we present the 3–σ upper/lower limits depending on each case. We also define the reflection fraction as $C_{\rm ref} = L_{\rm ref}/L_{\rm int}$ to quantify how much of the total flux corresponds to this emission. For this particular parameter, we establish the mean value after performing MCMC simulations within the parameter ranges as explained above.

An example of these spectral fits is represented in Fig. 5 for NGC 7582. We find that this object presents a non-negligible reflection component, since the preferred model is M_3. We also find that the reflection component is mainly detected through the Compton-hump, which accounts for $\sim 20\%$ of the intrinsic continuum. As mentioned above, our sample was selected such that the Eddington rate is in all cases $\lambda_{\rm Edd} < 10^{-3}$. However, this rate was calculated through the observed X-ray luminosity. Part of the analysis consists on correcting by absorption in the LOS. Fig. 6 (left) shows the the comparison between the observed 2-10 keV luminosity and the intrinsic 2-10 keV luminosity. The different symbols and colors correspond to different ranges of absorption as marked in the figure. The larger changes in luminosity occur for absorption along the line of sight in the Compton-thick (CT) regime (i.e., $\log(N_{\rm H}) > 24.17$) for which changes in the X-ray luminosity can be up to almost three orders of magnitude. Indeed, it is necessary to properly calculate the intrinsic luminosity of a source in order to characterize its Eddington rate and thus the efficiency. Note that the proper calculation of the luminosity moves the Eddington rate of our sample to higher values (see the right panel of Fig. 6), finding sources with Eddington rates of $\lambda_{\rm Edd} = 10^{-1}$. This shift shows that our sample is not complete in the range $-1 < \lambda_{\rm Edd} < 10^{-3}$ as we do not include low-obscured/unobscured sources with $\lambda_{\rm Edd} \sim 10^{-3}$. This issue is taken into account into

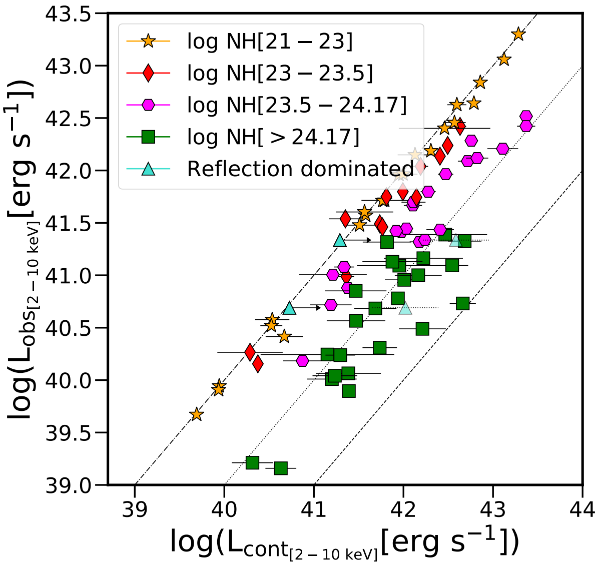

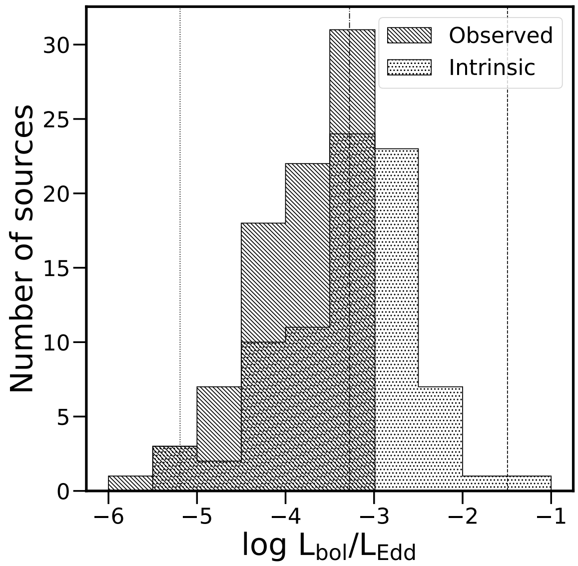

Figure 6: Left: Comparison between the observed and intrinsic 2-10 keV luminosities. The different symbols represent different ranges of obscuration, while the dotted-dashed, dotted and dashed lines represent correction factor from observed to intrinsic luminosity (i.e., a factor of 1, 10, and 100, respectively). The reflection dominated objects (cyan triangles) need this correction factor as the power-law is not detected with the X-ray spectra due to the domination of the reflection component. Right: Distribution of Eddington in our sample when it is calculated through the observed luminosity (dashed histogram) and when it is calculated through the intrinsic X-ray luminosity (dotted histogram).

the analysis.

As for the detection of the reflection in our sample, we define three criteria to establish the existence of this component: i) the likelihood of the M_3 model is statistically better compared to the simpler version M_1, which means that the M_3 model describes the spectra better than the M_1 model, statistically speaking. ii) The luminosity of the FeKα line is constrained at 1–σ. iii) The luminosity of the reflection component is also constrained at 1–σ.

Among our main results we find that most of our sources present signs of the reflection component. Indeed, around half of the sample (42 sources) fulfill all the three criteria above. For the remaining sources, only 10 sources present indications of the non-existence of this component, and thus the torus might have disappeared as expected from theoretical arguments (see the introduction), because none of the three criteria are fulfilled. The rest of the sample either has low S/N or a high obscuration which prevent us from detecting either the FeKα line or the Compton hump. Therefore, we cannot rule out that the reflection component is present for these objects. Moreover, two sources appear to be reflection dominated. This means that the intrinsic continuum is hidden under the reflection component (as can happen for very highly obscured sources). For both of them, we can extrapolate the intrinsic luminosity by assuming that for a certain line-of-sight obscuration, the intrinsic luminosity can be inferred from the luminosity of the reflection component, with the following approach: $\log(L_{cont}) = A + \log(L_{refl})$. The constant A can be calculated through the CT objects for which the power-law is still detected. We find in our analysis that $A = 1.3 \pm 0.4$. We apply the correction factor to these two sources in order to obtain the expected intrinsic X-ray luminosity for the subsequent analysis. This extrapolation corresponds to the the semi-translucent triangles in Fig. 6 (left panel).

We also aim to quantify the amount of reflection in our sample and how much of it that is represented by the FeKα line. Fig. 7 shows the correlations between the luminosity of the reflection component and that of the intrinsic continuum (left) and the FeKα line emission (right). The histograms in each figure represent the distribution in the range of luminosities for the sample. Note that the continuum intrinsic luminosity is spread over a wide range of luminosities, with a mean value of $L_{cont} = 10^{42.3}$ erg s^{-1}, while the mean value of the luminosity of the reflection component is $L_{ref} = 10^{42.0}$ erg s^{-1} and the mean value of the luminosity of the FeKα line is $L_{6.4keV} = 10^{40.2}$ erg s^{-1}. Also note that in either case, both quantities

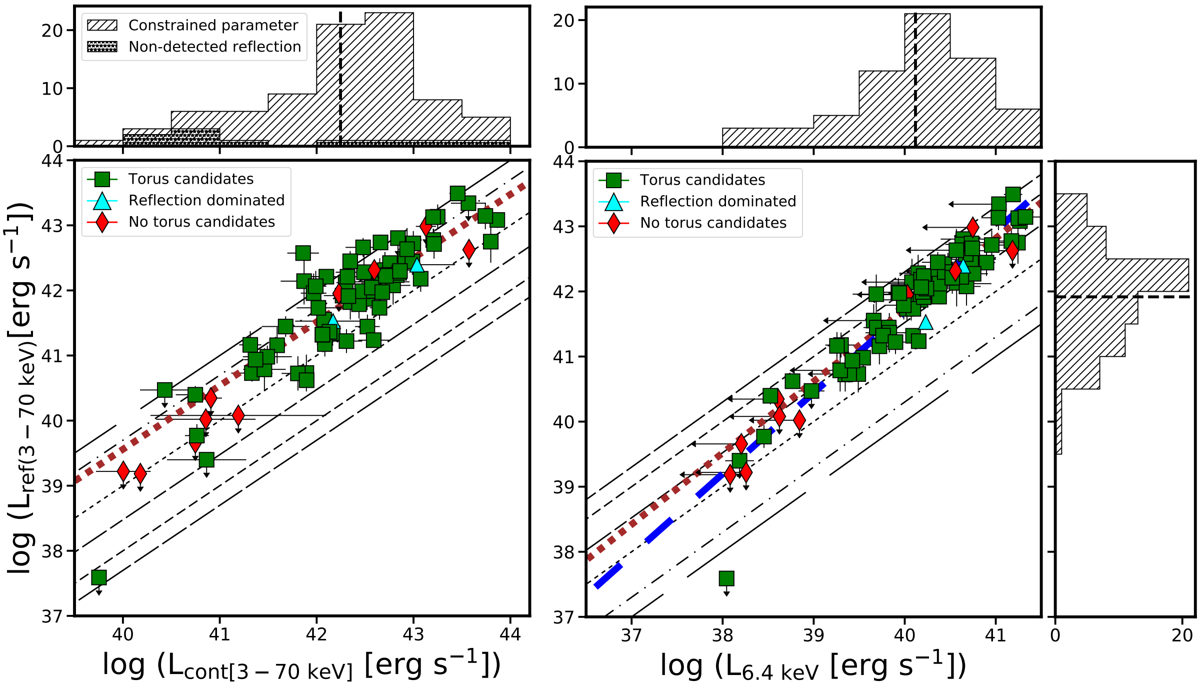

Figure 7: Left: The main panel shows the comparison between the luminosity of the reflection component and that of the intrinsic continuum. The top panel shows the distribution of the luminosity in our sample, where the dotted histogram represents the candidates for the torus disappearance. Right: Comparison between the luminosity of the reflection component and that of the FeKα emission line. The histograms on top and right show the distributions of each luminosity. The brown dotted lines in both panels represent the best-fit correlation between the Y axis and the X axis, when the X axis is the independent variable, while the dashed blue line in right panel is the best-fit correlation if the Y axis is the independent variable.

are well-correlated. We can quantify the correlations through the following equations:

$$\log(\mathrm{L_{ref}}) = (0.98 \pm 0.07)\log(\mathrm{L_{cont}}) + (0.40 \pm 3.16) \quad (5)$$

$$\log(\mathrm{L_{ref}}) = (1.10 \pm 0.05)\log(\mathrm{L_{6.4\ keV}}) - (2.26 \pm 2.12) \quad (6)$$

$$\log(\mathrm{L_{6.4\ keV}}) = (0.80 \pm 0.04)\log(\mathrm{L_{ref}}) + (6.54 \pm 1.61) \quad (7)$$

Note that these correlations do not account for upper/lower limits in the luminosities. Interestingly, the correlation between the intrinsic and reflection luminosities is consistent with the 1:1 relation, i.e., independently of the intrinsic luminosity, the amount of reflection is $\sim 60\%$ ($\mathrm{C_{ref}} = 0.57$). This can also be seen through the slope in Eq. 5. Contrary to this behaviour, the correlation between the reflection and the luminosity of the FeKα line seems to vary depending on the luminosity of the line emission (see Eq. 6). The amount of reflection seems to vary from 1% for a reflection luminosity luminosity of $\mathrm{L_{ref}} = 10^{43}$ erg s^{-1} to 5% at a reflection luminosity of $\mathrm{L_{ref}} = 10^{40}$ erg s^{-1}. We also test the scenario in which the independent quantity is the luminosity of the FeKα line, although we obtain that in either case, the correlation is not 1:1 (see Eq. 7).

We also check the level of obscuration in our sample. Interestingly, we find that the sources present values of obscuration which place them in a moderately to highly obscured regime. On average, the line-of-sight obscuration in our sample is $\log \mathrm{N_H} \sim 23.7$ cm^{-2}. Note that the 10 candidates for the torus disappearance have obscurations below this value and in some cases they even present upper limits, which indicates that the parameter cannot be constrained as it could be below the limits of the parameter in the spectral fitting. Our results are in general in agreement with previous works aiming to study the obscuration and the reflection in X-ray samples (Ricci et al., 2017) or even using different satellites (Kawamuro et al., 2016; Marchesi et al., 2018) for the objects in common. The discrepancies found in some cases can be due to the different physical models and torus geometries used in each analysis.

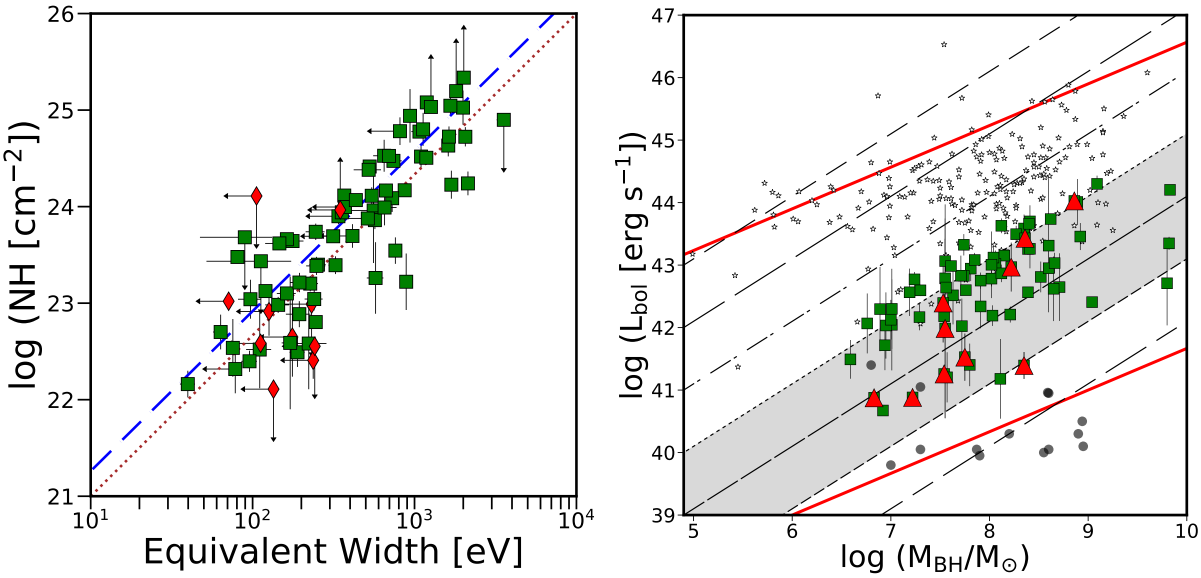

Figure 8: Right: Obscuration in the LOS versus equivalent width of the FeKα line. The red diamonds are our candidates for the torus disappearance. The brown dotted line is the correlation between the two quantities, while the blue dashed line is the expected correlation if both tracers come from the same region.

Another interesting result is the fact that both the equivalent width of the FeKα line and the LOS obscuration are correlated. Fig. 8 (left) shows this correlation. The red diamonds represent the candidates for the torus disappearance. These objects appear to present the smallest values for the equivalent width, with a few presenting upper limits. This correlation has been suggested for a long time (Leahy and Creighton, 1993), resulting from the assumption that the line-of-sight obscuration measured through X-rays comes from an uniformly shell of material surrounding the continuum sources. The spread in our sample can be explained through the different geometry and distribution of material in our case. Our sample presents in general high values for the line-of-sight obscuration. Furthermore, we present 18 CT sources, all of them with high amount of reflection component. An accurate measurement of the obscuration is necessary in order to properly calculate the intrinsic properties of the sources, which otherwise might lead to wrong conclusions on the efficiency and evolution. Overall, the expected percentage of CT sources in the nearby Universe is expected to be $\sim 23\%$ at $\lambda_{\rm Edd} \sim 10^{-5}$ (see Ricci et al., 2017; Marchesi et al., 2018), in agreement with the fraction found in our work, i.e., $\sim 20\%$.

Our results suggest a scenario with no obscuration for a large fraction of sources for lower Eddington rates, which is in agreement with the idea that both the BLR and the torus disappear for the least efficient sources as proposed by Elitzur and Shlosman (2006); Elitzur and Ho (2009); Elitzur and Netzer (2016), in which these regions are formed from a wind coming off the accretion disk. Thus, if the accretion disk is not expelling material in the necessary rate for the radiation field to counteract the gravitational force from the SMBH, both structures eventually collapse. However, prior to the full collapse and disappearance, the torus becomes denser and thus the column density increases, up to the point where it eventually disappears (thus no obscuration). Indeed, all our sources appear to be on average, more obscured than those from e.g., the *Swift*/BAT sample, except for our 10 candidates for the torus disappearance. Therefore, our findings are in agreement with the idea that as the object becomes less efficient, the X-ray features associated with the torus become fainter, and the reflection component is no longer traceable.

Fig. 8 (right) shows the bolometric luminosity versus black-hole mass diagram for our sample (red triangles and green squares), compared to the sources from the BASS sample Ricci et al. (2017) (blank stars) and the candidates for the torus disappearance through the infrared point of view sample from González-Martín et al. (2017) (gray circles). The red lines in the diagram show the region in which the torus may or may not exist depending on the wind parameters as proposed by Elitzur and Ho (2009). Note that our sources fall in this region. However, we do not find any source below this region, opposite to the results by González-Martín et al. (2017). Indeed, in their analysis, they find evidence for the torus disappearance for 11 objects, as seen from the mid-infrared. The difference relies on the fact that we may be missing less luminous sources as they might have not been observed yet due to their X-ray faintness. We also delimit the area between $10^{-5} < \lambda_{\rm Edd} < 10^{-3}$, i.e., the region in which we are certain to have completeness in the sample (gray shadowed area). Above $\lambda_{\rm Edd} \sim 10^{-3}$ we might be missing low-obscured/unobscured sources and we can not make strong conclusions in the region above. Our findings also suggest a scenario in which the strength of the FeKα line increases compared to the luminosity of the reflection component as long as the intrinsic luminosity of the source decreases and the Compton-hump scales with the intrinsic luminosity, suggesting an evolution on the chemical properties of the torus. This idea is in agreement with González-Martín et al. (2017), in which a group of sources with low torus contribution are not well described by the clumpy torus models at mid-infrared wavelengths. Thus, out of the scope of this thesis, we plan to apply for new *NuSTAR* dedicated observations to extent toward lower luminosity AGN to explore the obscuration signatures and the torus disappearance at even lower Eddington rate.

This work has already been sent to the *Monthly Notices of the Royal Astronomical Society* and we have already received the first report, which we are currently working on. The manuscript corresponding to this work is attached to this document.

4 AGNs from the CALIFA sample

Regarding the second part of the PhD project, in this section we describe the advances achieved up to this point together with the work that is still in development.

4.1 Sample selection

Our sample selection starts by searching in the CALIFA database (Sánchez et al., 2012). We selected the 906 galaxies observed within the framework of the CALIFA colaboration that fulfill the primary selection criteria (i.e., its optical extension is fully covered by the field-of-view of the adopted IFU (PPAK Kelz et al., 2006). The mean redshift of the sample is $z \sim 0.02$. We retrieve the coordinates of these sources and search all the available observations within the *Chandra* database, in the vicinity of these galaxies (with a search radius of two arcmin) keeping only those with exposure times larger than 5 ksec to ensure a minimum threshold for the source detection. We find 1366 observations for 247 galaxies. However, after processing, for 108 of these objects the coordinates fall outside the chip. Therefore, our initial sample contains a total of 139 galaxies for this analysis. We further exclude M 87 since the jet emission contaminates the X-ray spectrum and this particular source has been extensively studied with all X-ray satellites.

In order to ensure that we study the same source from X-rays and optical wavelengths, we compare the coordinates from the *Chandra* observations from those of the r filter of PANStarrs. This telescope is continously mapping the sky and searching for new objects, and at the same time producing accurate astrometry and photometry of already detected ones. We use these optical data becase CALIFA astrometry was corrected to match with them. The astrometry correction is motivated by the fact that galaxies in the CALIFA extended sub-sample (1/3 of the total sample nowadays) do not necessarily fit with the SDSS footprint. Therefore, there is no available SDSS data for all the targets. In order to provide with an homogeneous astrometry, the CALIFA observations were registered to the PANStarrs ones (Sánchez, priv. comm.). We compare the images from PANStarrs with the 0.5-10.0 and the 2.0-10.0 keV X-ray emission (see Section 4.2 for the data reduction procedure) for each of the sources. In the cases in which both coordinates do not match or are separated by more then 3 arcsec (which is the aperture used for *Chandra* nuclear spectral extractions), we correct the X-ray extraction to encircle the central emission. Fig. 9 shows an example of this comparison for the object NGC 0023. The gray-scale image corresponds to the PANStarrs image while the magenta contours correspond to the *Chandra* X-ray image in the full (left) and hard (right) bands, respectively. In both cases, the white dots are the coordinates retrieved from the NED database, whereas the cyan dots correspond to the CALIFA/PANStarrs astrometry corrected coordinates. In general, we find that most sources are well centered or the coordinates are separated less than 3 arcsec. In total, we corrected the coordinates for the central aperture extraction of nine sources (NGC 0890, NGC 1129, NGC 3395, NGC 3860, NGC 6166NED01, PGC 008502, PGC 033423, and UGC 04414).

We also check if our selection criteria could represent a bias for the analysis. For this reason, we compare the distribution of our sample in the BPT diagrams with that of the full CALIFA sample. Fig. 10 shows this comparison using the three classical diagnostic diagrams. Note that our sample (star symbols) are distributed throughout all the ranges, similar to the case of the full CALIFA sample (semi-

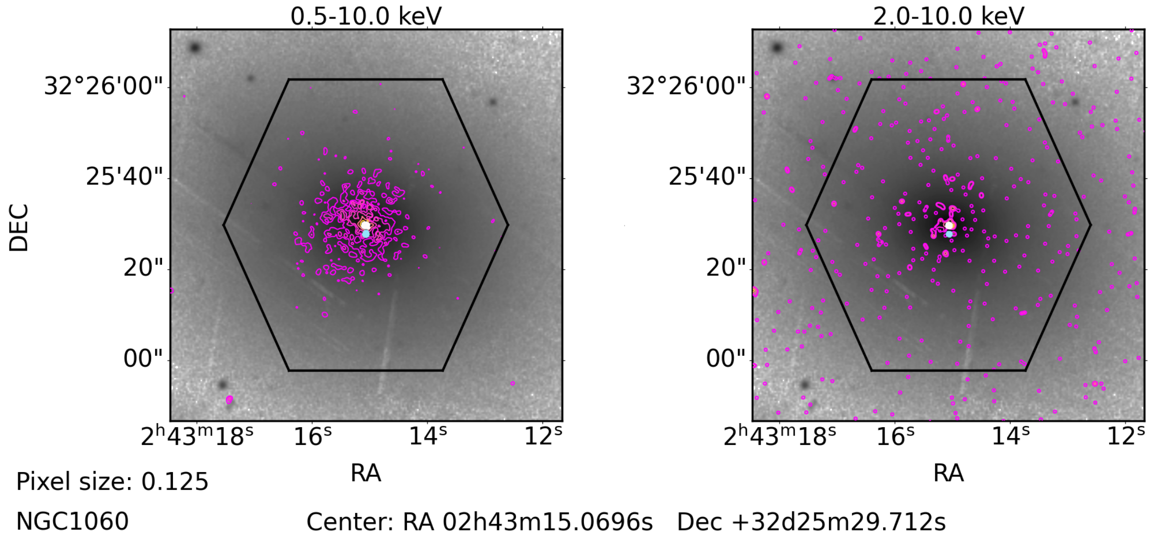

Figure 9: Comparison between the coordinates reported for each object in the optical and X-rays. Gray-scale corresponds to the PANStarrs r-band filter while the magenta contours correspond to the X-ray total (0.5-10.0 keV, left) and hard (2.0-10.0 keV, right) band images from *Chandra* for NGC 1060. The white and cyan dots correspond to the NED and CALIFA coordinates, respectively, whereas the black hexagon corresponds to the CALIFA field of view.

translucent circles). From a visual comparison, the only possible bias is the fact that X-ray detected sources seem to populate the right-wing area of the diagram in the left panel of the figure. To quantify this, we also perform a Kolmorogov-Smirnov (KS) test on the BPT diagram distribution. This test evaluates the probability of both samples being drawn from the same distribution. We obtain a p-value of 0.33, which indicates that both samples are not significantly different. On the other hand, Fig. 11 (left) shows the distribution of the EW of Hα for the full CALIFA sample (light gray) compared to the X-ray sub-sample (purple) and the Lacerda et al. (2020) AGN sample (dark gray). We also perform a KS test on the distribution of the EW of the Hα emission line, comparing both samples and obtain a p-value of 0.017, which means that our sample is slightly biased compared to the full CALIFA sample. This might be due to the fact that X-ray satellites are dedicated to find highly energetic phenomena, including nuclear activity, thermal contribution from galaxy clusters or high star-formation events. In contrast, optical wavelengths can identify normal galaxies. Thus, we expect that this approach induces some bias as the one seen here.

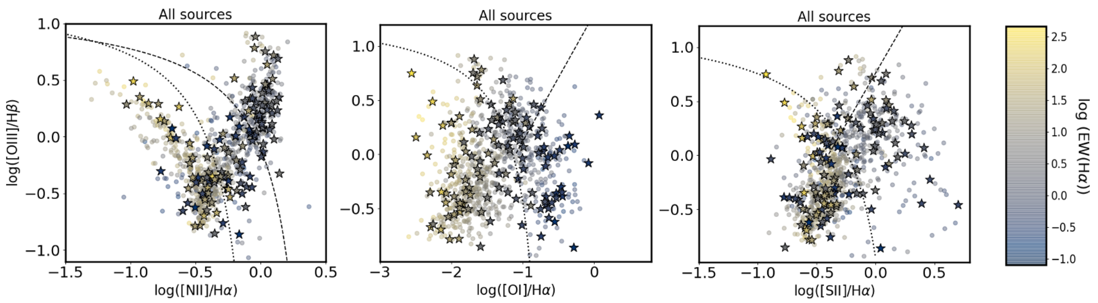

Figure 10: BPT diagrams for our sample (star symbols) in comparison with the full CALIFA sample (semi-translucent dots).

We also compare our sample with that from Lacerda et al. (2020), which contains identified AGN in the CALIFA sample. We have nine sources in common with their optically classified AGN (namely NGC 0833, NGC 2639, NGC 3861, NGC 5216, NGC 5675, NGC 5929, NGC 6251, UGC 03995 and UGC 1859). Out of these nine objects, three have X-ray emission in the central-source extraction only (NGC 0833, NGC 5216 and UGC 03995), one has X-ray emission in the ring-extraction only (NGC 3861), four have X-ray emission in both regions (NGC 2639, NGC 5675, NGC 5929 and NGC 6251), and one has not been detected so far, at least with *Chandra* (UGC 1859). In this case, the p-value of the KS test is $2.9e^{-6}$, which means that both samples are indeed different. Note that the selection of both samples are based on different procedures, so the fact that the two are statistically different from one another is not unexpected. For instance, Lacerda et al. (2020) selected AGN candidates based on their location in the BPT diagrams plus the value of the EW(Hα) for the values extracted at the center of the considered galaxies. However, the work done by Lacerda et al. (2020) is further used to compare it with our X-ray selected AGN (see below). Indeed, when comparing the EW distribution of their work with our sample or the full CALIFA, we find that their AGN have larger EW, while our sample contains both large and small values for this parameter.

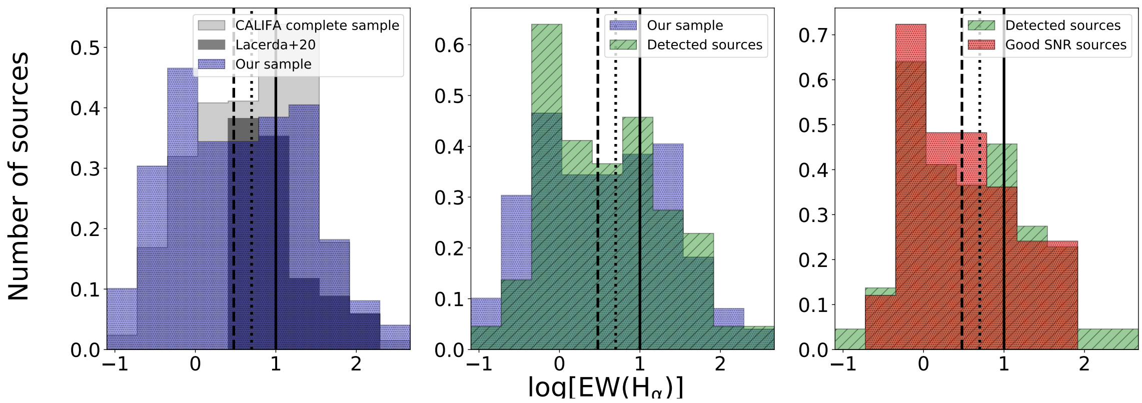

Figure 11: Left: distribution of equivalent widths for the full CALIFA sample (light gray), the Lacerda et al. (2020) AGN sample (dark gray) and our X-ray sample (138 sources, purple). Middle: our sample of 138 sources in comparison with the detected sources in the case of the central extraction (green). Right: detected sources in contrast with the sources with good SNR (orange). Note that there seems to be a majority of sources with small values of log |EW(Hα)|. In all the panels, the dashed and solid lines represent the region in which the galaxies in the green valley (hosting AGN) exist according to Lacerda et al. (2020), while the dotted line represents the limit of 6 Å as suggested by Stasińska et al. (2008); Cid Fernandes et al. (2011).

4.2 Data reduction

All the observations were processed using the *CXC Chandra Interactive Analysis of Observations* (CIAO[2]) software version 3.1. Our analysis is divided in two parts: i) study of the central region and ii) study of the diffuse/extended emission. In this section we explain how both regions were processed.

For the central source, we extract a circular region of 3 arcsec, which includes above 90% of the *Chandra* Point Spread Function (PSF) at the full energy band, and at the same time avoids contamination from extra-nuclear sources. For the background extraction, we produce different regions at distances between 4 and 7 times the radius of the central source extraction (i.e., 3 arcsec) and with position angles of 0, $\pm10, \pm20, \pm30, \pm40, \pm50, \pm60, \pm70, \pm80$ and ±90 degrees. We select the background region that ensures the maximization of the signal-to-noise ratio (SNR). We also remove the flaring background periods with the `deflare` task to exclude periods of high solar activity in our observations. We find a total of 63 objects with significant detection, i.e. with SNR>3. Thus, 45% of the sample has nuclear detection. Moreover, the subsequent spectral analysis will be performed for good SNR spectra, i.e. spectra with over 100 counts and more than 10 bins in the 0.5-10.0 keV X-ray band. We find 23 objects (16.5% of the sample) fulfilling this criterion for the central source.

For the extended/diffuse emission, we first define an annular region of inner radius 3 arcsec and outer radius 25 arcsec (the latter corresponding to the spatial resolution of *XMM*-Newton since our plan is to extend the analysis using this satellite, see Section 5). For the background selection, we also define an annular region with an inner radius of 30 arcsec outer radius 40 arcsec. However, we notice that this homogeneous extraction presents two important issues: i) the extended emission is not uniform in all the

[2] `http://asc.harvard.edu/ciao`

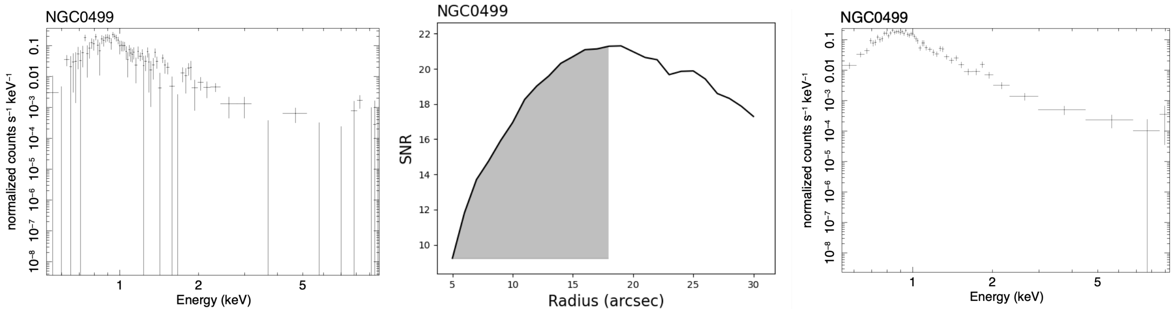

Figure 12: Left: spectrum of the extended emission for NGC 0499 when the annular extracted region is fixed to 3-25 arcsec, and the background is extracted as an annular region of inner radius 30 arcsec and outer radius 40 arcsec. Center: signal-to-noise ratio for NGC 0499 taking different outer radii for the extended emission. The peak of SNR is located at 18 arcsec, radius that will be used in the spectral analysis. Right: spectrum of the extended emission for NGC 0499 when the annular extracted region and its background are chosen to maximize the SNR.

sources, and it does not extend up to the same distances (i.e., some sources present significant extended emission while others rather present extra-nuclear component, and in other cases, the emission is not uniformly distributed in a ring-like shape) and ii) the background is not uniform for all the observations. Thus, this first extraction produces noisy spectra in most cases, one example shown in Fig. 12 (left) for the case of NGC 0499. To fix this problem, we extract annular regions with inner radius of 3 arcsec in all cases but with a variable outer radius from 5 to 30 arcsec in steps of 1 arcsec. We calculate the count-rate in all the regions and choose the region that maximizes the SNR. Fig. 12 (center) shows this calculation for NGC 0499, for which the optimal SNR outer radius is 18 arcsec. Thus, the spectral analysis of the extended/diffuse emission will be performed in this particular source for a ring from 3 to 18 arcsec. The optimal radius for each of the sources with enough SNR to make this analysis is listed in Tab. 4. Fig. 12 (right) clearly illustrates the improvement in the quality data of the extracted spectra when the size of the our ring is selected to maximize the SNR following the described procedure.

For the background selection, we first keep the background geometry fixed as an annular region, with the inner radius 10 arcsec larger than the outer radius of extended emission region. However, the spectra are still very noisy. We then perform an analysis similar to the one adopted to select the background for the central aperture extraction. We select circular regions with radius of 60 arcsec, but for which the center can be from from 120 to 210 arcsec far from the central coordinates. This radius is chosen to be bigger than the outer radius of the annular region in all cases. We also try different position angles and choose the region that maximizes the SNR of the background. In some cases, this causes the background region to be outside the chip. In these cases, we manually re-select the background in an emission-free region within the chip (this is done for 10 sources).

Despite all these detailed analysis, we still have some issues at the high-energy end of some spectra. This can be appreciated in Fig. 13 (left), there is an upturn above 7 keV in the spectrum of NGC 2748, which has no physical interpretation. This might be due to some issues regarding the calibration of the background. In order to investigate this, we selected a background free of emission, with different aperture radii and we extract it, subtracting the same background used for the diffuse/extended emission of the source. We found a non negligible contribution at energies below 1 keV and above 7 keV. We then model this background spectrum to characterize it and, therefore, subtract this instrumental issue from our analysis when needed. So far, the baseline model that we use for this background remnant is composed by two power-laws, with photon indices $\Gamma_1 = 20$ and $\Gamma_2 = -10.89$. We expect for this contribution to be negligible in most sources, but in those in which it is significant, this model will be added as a fixed component in the spectral analysis. For instance, the contribution for NGC 2748 seems to be roughly $\sim 10\%$ at 9 keV (data above 9 keV are neglected as the background dominates in all cases). The spectral fit of this background added to the extended emission can be seen in Fig. 13 (right). The pink and green lines are the two power-laws corresponding to the background remnant, while the black dotted line is the model associated with the extended emission (see sec. 4.4).

In summary, we find 65 objects with detection above the 3-σ level in the ring extraction corresponding to the extended/diffuse emission (i.e., 47% of the sample). Out of the 65 objects, 42 show central source emission as well. Moreover, we find that 45 observations out of these 65 (32% of the sample) have enough

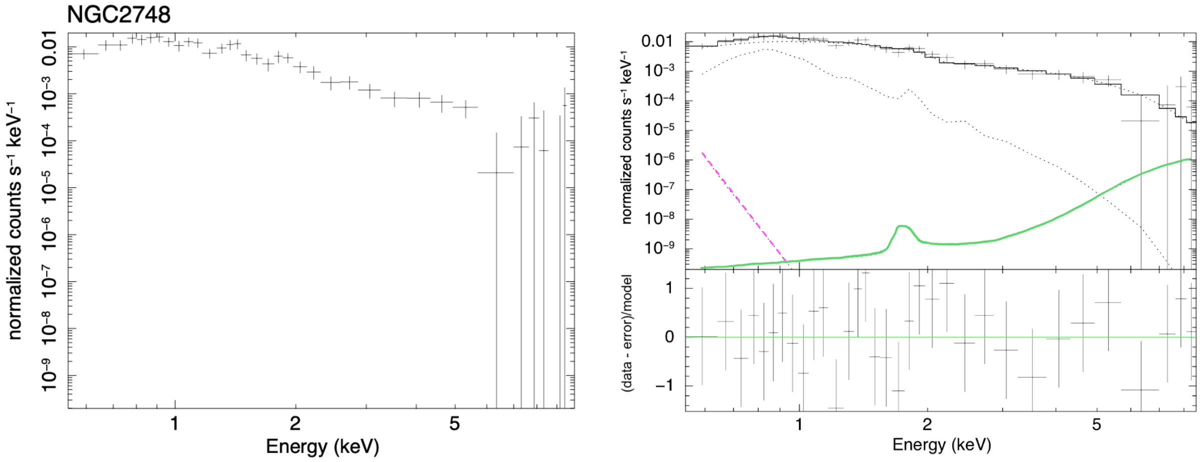

Figure 13: Left: spectrum of the extended emission for NGC 2748 showing an odd upturn around 6-7 keV which has to be properly accounted for before modelling the extended emission. Right: Spectral modelling of the extended emission, accounting for the background correction. Both pink and green lines correspond to the power-laws associated with the background calibration issue (convoluted by the response matrix of the instrument) while the black dotted line corresponds to the model applied to the extended emission (composed by thermal and non thermal emission, see Section 4.4).

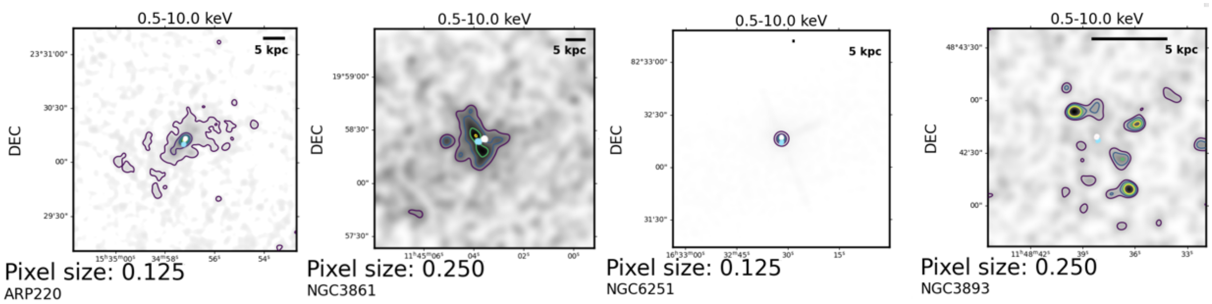

Figure 14: X-ray imaging classification of ARP 220 (left), NGC 0384 (center left), NGC 6251 (center right) and NGC 3893 (right). The white and cyan dots represent the NED and CALIFA coordinates. Note that in the case of ARP 220, there is extended + point-like emission, while in the case of NGC 0384 there is only extended emission and in the case of NGC 6251 there is point-like emission only. In all panels, the magenta, purple, blue, cyan, green and yellow contours correspond to 1%, 10%, 30%, 50%, 80% and 99% of the flux above the 3$-\sigma$ level.

SNR to perform the spectral analysis, out of which 23 also present good SNR spectra for the central source as well. In total, we find 85 objects with detection in either the central source, extended emission or both. Moreover, 45 objects have good SNR spectra in the central source, extended emission, or both. In addition, 53 sources do not present X-ray detection or emission.

4.3 Preliminary results

After determining how many observations have detected nuclear/extended emission, we have made an attempt to classify their X-ray morphology. For this purpose we create images in three energy bands: i) 0.5-2.0 keV, ii) 2.0-10.0 keV and iii) 0.5-10.0 keV. We apply a Gaussian filter to smooth the images and define contours above 3$-\sigma$ level. We classify the emission in four categories: i) point-like, ii) extended, iii) extended + point-like, and iv) extra nuclear sources. Fig. 14 shows an example of the characterization of the X-ray emission for ARP 220 (left), NGC 3861 (center left), NGC 6251 (center right) and NGC 3893 (right). We show these objects as examples of extended + point-like (left), extended (center left), point-like (center right) and extra-nuclear sources (right) emission in our sample.

Table 1 shows a summary of the preliminary results we obtain with this classification for both the central source and ring extractions. In total we find 37 objects with extended + point-like emission, eight objects with extended emission only, 29 objects with point-like emission only, and 11 objects with

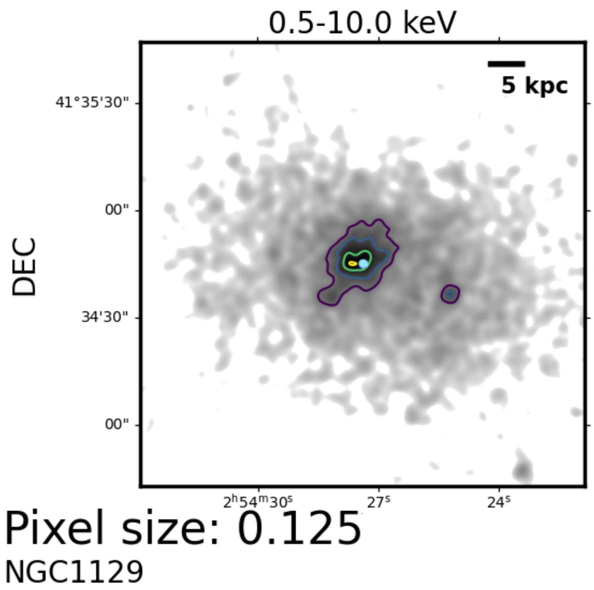

Figure 15: X-ray morphological analysis for NGC 1129. This object presents detection in both the central source and extended emission extractions, and it appears to have extended emission only, although a proper analysis of the PSF has to be done before deriving any conclusion on its morphology. The contours are the same as in Fig. 14.

off-nuclear sources. This table clearly shows that our visual classification presents some contradictions with the quantitative analysis done previously based on the detection at the ring, central aperture or both. For instance, among the objects with central source detection only (from the quantitative analysis), there are two objects presenting extended + point-like emission. This is probably due to the fact that we determine the extended emission from 3 arcsec toward larger radii, while the extended emission found in our visual analysis might be closer than 3 arcsec from the nucleus. Our plan is to perform a more robust identification of nuclear and extended emission based on the fit of the radial profile including the *Chandra* PSF. Once we quantify the amount of emission corresponding to the PSF, we will be able to define whether it is extended or point-like emission in a more accurate way.

Among those sources with detection in both the central aperture and ring extractions (from our quantitative analysis), there are four objects that we visually classified as extended emission only. One of these objects (NGC 1129) is shown as an example in Fig. 15. From the quantitative analysis, it has emission in both central and ring extractions. However, from the visual analysis, it appears to have extended emission only. Again, we believe that we need to fit the emission to a radial profile and quantify the amount of emission corresponding to a point-like profile to ensure the detection of nuclear point-like emission in such diffuse-dominated morphology.

Region	Detections				SNR
	Ext. + point-like	Extended	Point-like	Extra-nuclear sources	
(1)	(2)	(3)	(4)	(5)	(6)
Ring only	8	3	0	11	22
Central source only	2	0	19	0	0
Both	36	4	2	0	23

Table 1: Col. (1): Extracted region. Cols. (2)-(5): Distribution of sources with emission in the ring extraction, central extraction and in both regions. Col. (6) Distribution of sources with good SNR for the spectral analysis, in the total 0.5-10.0 keV band.

One of our goals is to understand the differences between the optical and X-rays classifications. For that purpose we have done a preliminary analysis on the BPT diagrams to study the position of our X-ray detected nuclear sources in these BPT diagrams. Fig. 16 shows the location of our sample in the [NII] vs [OIII] BPT diagram, compared to the full CALIFA sample. In this case, the reported values from

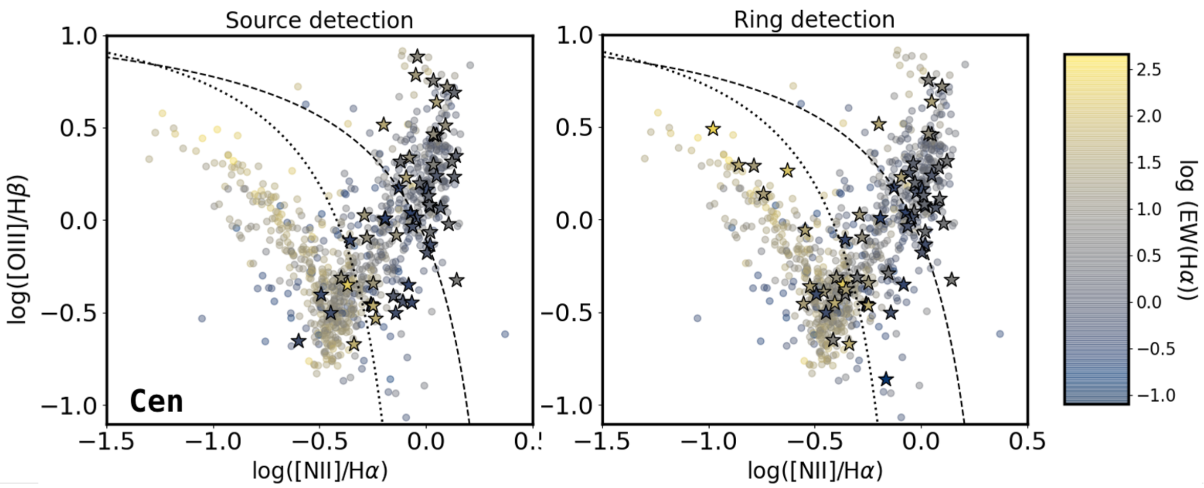

Figure 16: BPT diagram for our sample (star symbols) in comparison with the complete CALIFA sample (semi-translucent circles). The left panel shows those sources for which the central source extraction has detection, while the right panel shows the sources for which the ring extraction (associated with extended/diffuse emission) has detection. The line measurement in all sources correspond to the value reported for the central region of the galaxies Lacerda et al. (2020).

CALIFA we use are those corresponding to the central region (i.e., where an AGN would be located). However, we also investigate the behaviour of the sources with measurements in other regions of the galaxy such as the effective radius and the complete galaxy. Indeed, we find similar behaviour in the distribution of objects in this diagram, for both the effective radius and complete galaxy measurements (see Fig. 17). The left panel of the figure shows the full CALIFA sample (semi-translucent circles) and our X-ray selected AGN candidates (star symbols). Note that this is preliminary because we need to clean the X-ray selected AGN according to the radial profile analysis (to ensure the detection of a point-like source coincident with the nucleus) and the information obtained from the spectral analysis (see below). However, it is worth to notice that most of the detected X-ray sources seem to be on the right wing of the BPT, although with EW($H\alpha$) values spanned throughout all the range.

Interestingly, we detect X-ray sources down to the area where both wings merge. This might mean that AGN embedded in circumnuclear HII regions are not easily found with these diagrams but can be isolated from X-rays. We also compare the BPT diagrams for the extended/diffuse emission extractions (see right panel in Fig. 16). Note that in this case, objects seem to populate both the AGN and the HII wings of the diagram, although this has to be further analyzed before deriving any conclusion. For instance, X-rays are also observed in shocks associated with outflows and galactic winds. Thus, a match between those targets and the outflow candidates by López-Cobá et al. (2019) should be considered. Interestingly, although not included in this report, we also explore the other optical diagnostic diagrams, finding that the X-ray detected objects objects tend to be located all over them. This might indicate that the BPT diagram shown in Fig. 16 is better to catch X-ray selected AGN. However, further analysis is needed in order to confirm this scenario. For instance, the locus of X-ray selected from the spectral analysis are required to further restrict our selected AGN.

4.4 Future work

The future work for this project is divided in two parts:

A. Extended/diffuse soft X-ray emission: For the morphological analysis, we will use different emission line images from CALIFA and compare their morphology with the X-ray images in order to study whether both emissions come from the same spatial region. This will help us understand the origin of the extended emission in our objects. Plausible origins are: star-forming regions, hot thermal plasma from the inter galactic medium (IGM), AGN NLR, or shocks associated with outflows Some spatial analysis has been performed before (Yan et al., 2011; Bianchi et al., 2012; Gómez-Guijarro et al., 2017), where they conclude that both the X-ray and optical emission may come from nuclear ionization. However, these analyses do not include non-AGN galaxies in their statistics. Additionally, we will be able to explore other optical tracers thanks to the information provided by the CALIFA datacubes. Indeed, we will use the bi-dimensional BPT diagrams using the emission lines in CALIFA, to compare SF and

AGN-ionized region according to these diagrams. Note that this project takes advantage of the spatial resolution provided by *Chandra* which is much better in comparison with the other X-ray satellites that will be used in this analysis. Finally, the results of this work will be published in a scientific paper.

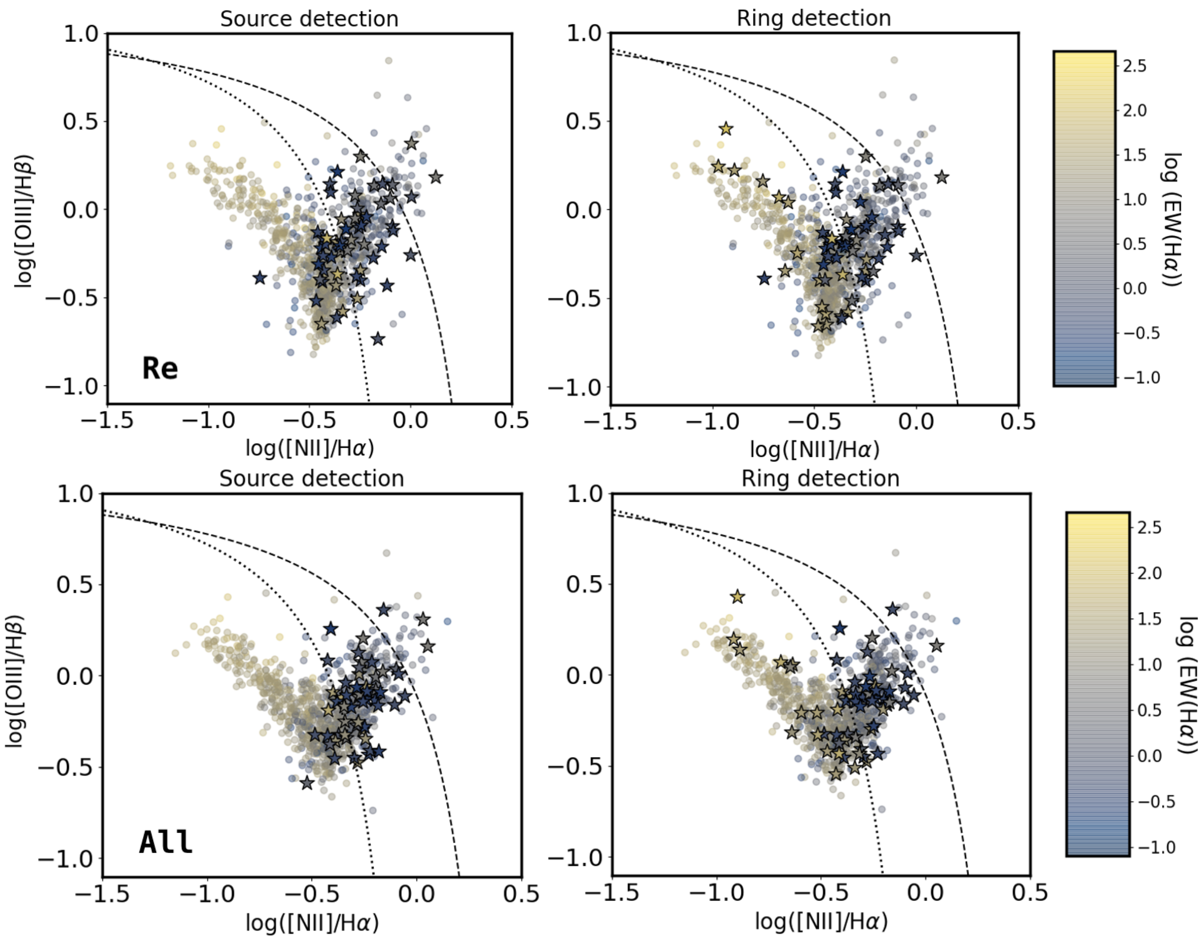

Figure 17: BPT diagrams for the line ratio measurements in the effective radius (top) and in the complete galaxy (bottom) (Espinosa-Ponce et al., 2020).

B. AGN in the CALIFA sample: We already have a morphological analysis of the sample. However, a spectral analysis is mandatory to understand the true nature of our sources. The X-ray spectra can provide definitive proves of the AGN nature as a hard power-law spectrum, the luminosity of the source, or the existence of the FeKα emission line.

For the X-ray spectral analysis we will use several satellites (see below). *Chandra* spatial resolution will allow us to characterize the extended emission to subtract it from low-resolution spectra. For that purpose, we need to fit both the central source and ring extractions to a set of models, which account for different physical scenarios regarding the nature of the sources, among the models we find:

$$M_1 = \texttt{phabs}_{\rm Gal}(\texttt{pcfabs} * \texttt{powerlaw}) \quad (8) \qquad M_2 = \texttt{phabs}_{\rm Gal}(\texttt{apec}) \quad (9)$$

$$M_3 = \texttt{phabs}_{\rm Gal}(\texttt{bbody}) \quad (10) \qquad M_4 = \texttt{phabs}_{\rm Gal}(\texttt{apec} + \texttt{pcfabs} * \texttt{powerlaw}) \quad (11)$$

where Eq. (8) is expected for AGN emission as the accretion disk emits as a power-law, for which the photon index gives hints on the accretion state of the source and the partial-covering scenario (`pcfabs`) accounts the obscuration from the clouds around the accretion disk. Eq. (9) has a thermal component, representing ionized diffuse gas emission, which is expected for AGNs with extended emission, probably linked with the host galaxy. Eq. (10) is a simple black-body representing the non-AGN scenario. Eq. (11) is a combination of (8) and (9), representing the combination of extended and AGN emission. These spectral models are simple but they will certainly help to access the nature of the sources and ideal for the expected low SNR for *Chandra* spectra.

As we already mentioned, we want to extend our study to other X-ray satellites. In particular we plan to extend the analysis to *XMM*-Newton and *NuSTAR* to achieve better SNR spectra for the current sample and to enlarge the number of sources with X-ray observations from the CALIFA sample. For this purpose, we will search for observations of our AGN sample. From a preliminary search, we find that 92 sources have observations in either *XMM*-Newton or *NuSTAR*, but we will update the sample with a new search in both databases. We will reduce the data, extract spectra, and fit the data to different physical models. We will account for the extended emission when necessary. For this purpose, we will use the best-fit model from the *Chandra* data fixed to the *XMM*-Newton and *NuSTAR* data if available. We will add circumnuclear spectral components otherwise. Note that we plan to make more complex spectral analysis for these satellites. In particular, *NuSTAR* will require a proper analysis of the reflected component described in section 3 of this document. Therefore, we expect to add the models used in the first part of the project, represented by Eqs. (1-4). This will allow us to model the full X-ray band (0.5-79 keV) spectra of the sources, which is necessary to derive conclusions on the nature of these objects.

The final aim of this part of the project is to give hints on the fraction of AGN in the CALIFA sample, and to compare the X-ray classification with the optical one, and to study if AGN are located in the green valley. The results of this part of the project will be published in at least another paper.

5 Overall status of the project and updates

In this section we present the work to be done for the remaining of the PhD. For this purpose, we show below the initial activity schedule proposed to the academic committee, pointing out to the modifications that have been made along these three semesters as well as the goals to be fulfilled from now on.

✓ S1 We define the projects of the PhD. We also define the samples and will perform the data reduction corresponding to the first part of the project (torus evolution). I also study some literature related to both projects.

✓ S2 We perform the spectral fits necessary for the first project. We also prepare a draft for the first paper of the PhD with the results. We also expect to reduce the *Chandra* data and perform the morphological analysis of the sources. We expect to have a stay with Dr. Sebastián Sánchez at IA-CU to work on the CALIFA sample.

....

UPDATE: At the end of the first semester we were advise to extend the sample corresponding to the torus evolution in order to make it more complete, therefore requiring extra time in order to perform the data reduction. We also changed our initial sample and modified the selection criteria.

We also worked on the spectral model since some authors suggest that the inclusion of Compton-scatting absorption component is relevant, in particular for highly obscured object, when using data above 10 keV. We worked on new spectral fits and it took us around one month. However, later on the development of this project, we found that this spectral model had some physical issues and at the end we had to discard this analysis. Note that nonetheless, we were able to work on the first version of the paper. Regarding the CALIFA project, we also had to work out on the CALIFA sample to ensure that we had the best and most complete sample. Nonetheless, at the end of the semester we already had the data processed. The delay on the first project, postponed the data analysis of CALIFA sample to the next semester. Additionally, it was not possible to make the stay with Dr. Sebastián Sánchez mostly due the pandemic event.

✓ S3 We will send the first paper related to the torus evolution and we plan to attend an international conference to present the results from this work. We will also perform the spectral fits of the nuclear and circumnuclear contribution of the *Chandra* data for the CALIFA sample regarding the second project. We also expect to make a stay with Dr. Sebastián Sánchez in order to discuss the preliminary results regarding the morphological analysis of the data. This semester I present the candidature exam.

....

UPDATE: We finished the first version of the paper regarding the torus evolution, circulated among co-authors, and sent it to the *Monthly Notices of the Royal Astronomical Society*. We already received the referee report which suggested moderate revision. We plan to work on it as soon as this candidature exam finishes. While under the reviewing process, we worked on the morphological analysis of the sources from the CALIFA sample and also managed to make the spectral extraction of the nuclear and circumnuclear regions. However, in this latter part, we had an issue regarding the circumnuclear extraction. In particular, we initially had assumed an outer radius of 30 arcsec.

However, when we were analyzing the spectra in a quantitative way, we realized that not all sources should be treated equally. Therefore, we had to perform several ring extractions to ensure the maximum SNR in each case. We are currently developing the spectral analysis of the nucleus.

S4 We will make the corrections of the referee report. We will start writing a second paper with the morphological analysis from the CALIFA sample. We will download and process data from *XMM*-Newton y *NuSTAR* and perform the spectral analysis accounting for the circumnuclear contribution found with *Chandra* data.

. . . .

<u>UPDATE</u>: For this semester, it was also planned for me to attend to an international institution and give a talk there. However, we believe that this might be possible in the fifth semester as we have some work behind the schedule and perhaps it would be easier when the pandemic situation is under control. Additionally, outside of the scope of this thesis, we plan to request observing time in *NuSTAR* for the objects with the lowest luminosities as explained in section 3, and we will work on the proposal throughout this semester. Finally, we expect to be able to attend the Congreso Nacional de Física conference and share the results corresponding to the torus evolution project.

S5 We sill send the second paper regarding the morphological and spectral analysis of the CALIFA sample with *Chandra* data. We will create a new AGN catalogue with X-ray data and we will compare both the X-ray and optical properties of the objects.

. . . .

<u>UPDATE</u>: We expect to have the paper finished during this semester according to the plan. During this semester I also expect to have an international stay in a institution. We believe that an X-ray group is most convenient, for instance the IFCA X-gray group or someone from the *NuSTAR* collaboration. We also expect to finish the spectral fits corresponding to the *XMM*-Newton and *NuSTAR* data.

S6 We will answer to the referee report corresponding to the second paper and we will start developing a third draft with the spectral results from *Chandra*, *XMM*-Newton and *NuSTAR*. We will also start writing the dissertation and expect to attend to an international conference to our results from the CALIFA sample through X-rays.

S7 We will finish the third paper and will send it to a journal. The rest of the semester will be focused on writing the dissertation, which we expect to be on the modality of compilation of papers developed throughout the PhD.

S8 We will answer the referee report corresponding to the third paper. I will send the dissertation and answer to the jury corrections. Finally I expect to present the PhD defense during this semester.

We present below the initial timeline proposed to develop the PhD project and an updated version of the timeline to fulfill all the goals for the PhD thesis in Table 2.

INITIAL TIMELINE									CURRENT TIMELINE								
	S1	S2	S3	S4	S5	S6	S7	S8		S1	S2	S3	S4	S5	S6	S7	S8
Goal 1	⋆	⋆ ⋆	⋆	⋆					Goal 1	⋆	⋆ ⋆ ⋆	⋆	⋆				
Goal 2.1	⋆	⋆	⋆	⋆	⋆ ⋆	⋆			Goal 2.1	⋆	⋆	⋆ ⋆	⋆	⋆ ⋆	⋆		
Goal 2.2	⋆			⋆	⋆ ⋆	⋆	⋆	⋆	Goal 2.2	⋆			⋆	⋆ ⋆	⋆	⋆	⋆
Others	⋆	⋆	⋆ ⋆	⋆		⋆ ⋆	⋆⋆⋆	⋆⋆⋆	Others	⋆		⋆	⋆		⋆ ⋆	⋆⋆⋆	⋆⋆⋆

Table 2: Initial (left) and current (right) timeline of the project. Blue stars correspond to the development of each goal, while red stars correspond to bureaucratic processes and brown stars correspond to international meetings.

References

Annuar, A., Alexander, D. M., Gandhi, P., Lansbury, G. B., Asmus, D., Ballantyne, D. R., Bauer, F. E., Boggs, S. E., Boorman, P. G., Brandt, W. N., Brightman, M., Christensen, F. E., Craig, W. W., Farrah, D., Goulding, A. D., Hailey, C. J., Harrison, F. A., Koss, M. J., LaMassa, S. M., Murray, S. S., Ricci, C., Rosario, D. J., Stanley, F., Stern, D., and Zhang, W. (2017). A New Compton-thick AGN in our Cosmic Backyard: Unveiling the Buried Nucleus in NGC 1448 with NuSTAR. *ApJ* , 836(2):165.

Annuar, A., Alexander, D. M., Gandhi, P., Lansbury, G. B., Asmus, D., Baloković, M., Ballantyne, D. R., Bauer, F. E., Boorman, P. G., Brandt, W. N., Brightman, M., Chen, C. T. J., Del Moro, A., Farrah, D., Harrison, F. A., Koss, M. J., Lanz, L., Marchesi, S., Masini, A., Nardini, E., Ricci, C., Stern, D., and Zappacosta, L. (2020). NuSTAR observations of four nearby X-ray faint AGNs: low luminosity or heavy obscuration? *MNRAS* , 497(1):229–245.

Annuar, A., Gandhi, P., Alexander, D. M., Lansbury, G. B., Arévalo, P., Ballantyne, D. R., Baloković, M., Bauer, F. E., Boggs, S. E., Brandt, W. N., Brightman, M., Christensen, F. E., Craig, W. W., Del Moro, A., Hailey, C. J., Harrison, F. A., Hickox, R. C., Matt, G., Puccetti, S., Ricci, C., Rigby, J. R., Stern, D., Walton, D. J., Zappacosta, L., and Zhang, W. (2015). NuSTAR Observations of the Compton-thick Active Galactic Nucleus and Ultraluminous X-Ray Source Candidate in NGC 5643. *ApJ* , 815(1):36.

Antonucci, R. (1993). Unified models for active galactic nuclei and quasars. *ARA&A* , 31:473–521.

Baldwin, J. A., Phillips, M. M., and Terlevich, R. (1981). Classification parameters for the emission-line spectra of extragalactic objects. *PASP* , 93:5–19.

Bär, R. E., Trakhtenbrot, B., Oh, K., Koss, M. J., Wong, O. I., Ricci, C., Schawinski, K., Weigel, A. K., Sartori, L. F., Ichikawa, K., Secrest, N. J., Stern, D., Pacucci, F., Mushotzky, R., Powell, M. C., Ricci, F., Sani, E., Smith, K. L., Harrison, F. A., Lamperti, I., and Urry, C. M. (2019). BAT AGN Spectroscopic Survey - XIII. The nature of the most luminous obscured AGN in the low-redshift universe. *MNRAS* , 489(3):3073–3092.

Bennert, N. (2005). *The narrow line region of active galaxies*. Univ. Bochum. http://dx.doi.org/10.23689/fidgeo-135.

Bianchi, S., Panessa, F., Barcons, X., Carrera, F. J., La Franca, F., Matt, G., Onori, F., Wolter, A., Corral, A., Monaco, L., Ruiz, Á., and Brightman, M. (2012). Simultaneous X-ray and optical observations of true type 2 Seyfert galaxies. *MNRAS* , 426(4):3225–3240.

Cid Fernandes, R., Stasińska, G., Mateus, A., and Vale Asari, N. (2011). A comprehensive classification of galaxies in the Sloan Digital Sky Survey: how to tell true from fake AGN? *MNRAS* , 413(3):1687–1699.

Davidson, K. and Netzer, H. (1979). The emission lines of quasars and similar objects. *Reviews of Modern Physics*, 51(4):715–766.

Davies, R. L., Groves, B., Kewley, L. J., Dopita, M. A., Hampton, E. J., Shastri, P., Scharwächter, J., Sutherland, R., Kharb, P., Bhatt, H., Jin, C., Banfield, J., Zaw, I., James, B., Juneau, S., and Srivastava, S. (2016). Dissecting galaxies: spatial and spectral separation of emission excited by star formation and AGN activity. *MNRAS* , 462(2):1616–1629.

Elitzur, M. and Ho, L. C. (2009). On the Disappearance of the Broad-Line Region in Low-Luminosity Active Galactic Nuclei. *ApJL* , 701(2):L91–L94.

Elitzur, M. and Netzer, H. (2016). Disc outflows and high-luminosity true type 2 AGN. *MNRAS* , 459(1):585–594.

Elitzur, M. and Shlosman, I. (2006). The AGN-obscuring Torus: The End of the "Doughnut" Paradigm? *ApJL* , 648(2):L101–L104.

Esparza-Arredondo, D., González-Martín, O., Dultzin, D., Ramos Almeida, C., Fritz, J., Masegosa, J., Pasetto, A., Martínez-Paredes, M., Osorio-Clavijo, N., and Victoria-Ceballos, C. (2019). Physical Parameters of the Torus for the Type 2 Seyfert IC 5063 from Mid-IR and X-Ray Simultaneous Spectral Fitting. *ApJ* , 886(2):125.

Espinosa-Ponce, C., Sánchez, S. F., Morisset, C., Barrera-Ballesteros, J. K., Galbany, L., García-Benito, R., Lacerda, E. A. D., and Mast, D. (2020). H II regions in the CALIFA survey: I. catalogue presentation. *MNRAS* , 494(2):1622–1646.

Ezhikode, S. H., Dewangan, G. C., Misra, R., and Philip, N. S. (2020). Correlation between relativistic reflection fraction and photon index in NuSTAR sample of Seyfert 1 AGN. *MNRAS* , 495(3):3373–3386.

Fanaroff, B. L. and Riley, J. M. (1974). The morphology of extragalactic radio sources of high and low luminosity. *MNRAS* , 167:31P–36P.

Ferrarese, L. and Merritt, D. (2000). A Fundamental Relation between Supermassive Black Holes and Their Host Galaxies. *ApJL* , 539(1):L9–L12.

Fritz, J., Franceschini, A., and Hatziminaoglou, E. (2006). Revisiting the infrared spectra of active galactic nuclei with a new torus emission model. *MNRAS* , 366(3):767–786.

Gebhardt, K., Kormendy, J., Ho, L. C., Bender, R., Bower, G., Dressler, A., Faber, S. M., Filippenko, A. V., Green, R., Grillmair, C., Lauer, T. R., Magorrian, J., Pinkney, J., Richstone, D., and Tremaine, S. (2000). Black Hole Mass Estimates from Reverberation Mapping and from Spatially Resolved Kinematics. *ApJL* , 543(1):L5–L8.

Gómez-Guijarro, C., González-Martín, O., Ramos Almeida, C., Rodríguez-Espinosa, J. M., and Gallego, J. (2017). A comparison between the soft X-ray and [O III] morphologies of active galactic nuclei. *MNRAS* , 469(3):2720–2736.

González-Martín, O., Masegosa, J., Hernán-Caballero, A., Márquez, I., Ramos Almeida, C., Alonso-Herrero, A., Aretxaga, I., Rodríguez-Espinosa, J. M., Acosta-Pulido, J. A., Hernández-García, L., Esparza-Arredondo, D., Martínez-Paredes, M., Bonfini, P., Pasetto, A., and Dultzin, D. (2017). Hints on the Gradual Resizing of the Torus in AGNs through Decomposition of Spitzer/IRS Spectra. *ApJ* , 841(1):37.

González-Martín, O., Masegosa, J., Márquez, I., Guainazzi, M., and Jiménez-Bailón, E. (2009). An X-ray view of 82 LINERs with Chandra and XMM-Newton data. *A&A* , 506(3):1107–1121.

González-Martín, O., Masegosa, J., Márquez, I., Rodríguez-Espinosa, J. M., Acosta-Pulido, J. A., Ramos Almeida, C., Dultzin, D., Hernández-García, L., Ruschel-Dutra, D., and Alonso-Herrero, A. (2015). Nuclear obscuration in LINERs. Clues from Spitzer/IRS spectra on the Compton thickness and the existence of the dusty torus. *A&A* , 578:A74.

Hasinger, G., Cappelluti, N., Brunner, H., Brusa, M., Comastri, A., Elvis, M., Finoguenov, A., Fiore, F., Franceschini, A., Gilli, R., Griffiths, R. E., Lehmann, I., Mainieri, V., Matt, G., Matute, I., Miyaji, T., Molendi, S., Paltani, S., Sanders, D. B., Scoville, N., Tresse, L., Urry, C. M., Vettolani, P., and Zamorani, G. (2007). The XMM-newton wide-field survey in the COSMOS field. i. survey description. *The Astrophysical Journal Supplement Series*, 172(1):29–37.

Heckman, T. M. (1980). An optical and radio survey of the nuclei of bright galaxies - Stellar populations and normal H II regions. *A&A* , 87(1-2):142–151.

Ho, L. C. (2008). Nuclear activity in nearby galaxies. *ARA&A* , 46:475–539.

Hönig, S. F. and Kishimoto, M. (2010). The dusty heart of nearby active galaxies. II. From clumpy torus models to physical properties of dust around AGN. *A&A* , 523:A27.

Hönig, S. F. and Kishimoto, M. (2017). Dusty Winds in Active Galactic Nuclei: Reconciling Observations with Models. *ApJL* , 838(2):L20.

Hopkins, P. F., Murray, N., and Thompson, T. A. (2009). The small scatter in BH-host correlations and the case for self-regulated BH growth. *MNRAS* , 398(1):303–311.

Kahre, L., Walterbos, R. A., Kim, H., Thilker, D., Calzetti, D., Lee, J. C., Sabbi, E., Ubeda, L., Aloisi, A., Cignoni, M., Cook, D. O., Dale, D. A., Elmegreen, B. G., Elmegreen, D. M., Fumagalli, M., Gallagher, J. S., I., Gouliermis, D. A., Grasha, K., Grebel, E. K., Hunter, D. A., Sacchi, E., Smith, L. J., Tosi, M., Adamo, A., Andrews, J. E., Ashworth, G., Bright, S. N., Brown, T. M., Chand ar, R., Christian, C., de Mink, S. E., Dobbs, C., Evans, A. S., Herrero, A., Johnson, K. E., Kennicutt, R. C., Krumholz, M. R., Messa, M., Nair, P., Nota, A., Pellerin, A., Ryon, J. E., Schaerer, D., Shabani, F., Van Dyk, S. D., Whitmore, B. C., and Wofford, A. (2018). Extinction Maps and Dust-to-gas Ratios in Nearby Galaxies with LEGUS. *ApJ* , 855(2):133.

Kalberla, P. M. W., Burton, W. B., Hartmann, D., Arnal, E. M., Bajaja, E., Morras, R., and Pöppel, W. G. L. (2005). The Leiden/Argentine/Bonn (LAB) Survey of Galactic HI. Final data release of the combined LDS and IAR surveys with improved stray-radiation corrections. *A&A* , 440(2):775–782.

Kang, J., Wang, J., and Kang, W. (2020). NuSTAR Hard X-Ray Spectra of Radio Galaxies. *ApJ* , 901(2):111.

Kauffmann, G., Heckman, T. M., Tremonti, C., Brinchmann, J., Charlot, S., White, S. D. M., Ridgway, S. E., Brinkmann, J., Fukugita, M., Hall, P. B., Ivezić, Ž., Richards, G. T., and Schneider, D. P. (2003). The host galaxies of active galactic nuclei. *MNRAS* , 346(4):1055–1077.

Kawamuro, T., Ueda, Y., Tazaki, F., Terashima, Y., and Mushotzky, R. (2016). Study of Swift/Bat Selected Low-luminosity Active Galactic Nuclei Observed with Suzaku. *ApJ* , 831(1):37.

Kelz, A., Verheijen, M. A. W., Roth, M. M., Bauer, S. M., Becker, T., Paschke, J., Popow, E., Sánchez, S. F., and Laux, U. (2006). PMAS: The Potsdam Multi-Aperture Spectrophotometer. II. The Wide Integral Field Unit PPak. *PASP* , 118(839):129–145.

Kewley, L. J., Dopita, M. A., Sutherland, R. S., Heisler, C. A., and Trevena, J. (2001). Theoretical Modeling of Starburst Galaxies. *ApJ* , 556(1):121–140.

Kewley, L. J., Groves, B., Kauffmann, G., and Heckman, T. (2006). The host galaxies and classification of active galactic nuclei. *MNRAS* , 372(3):961–976.

Khorunzhev, G. A., Sazonov, S. Y., Burenin, R. A., and Tkachenko, A. Y. (2012). Masses and accretion rates of supermassive black holes in active galactic nuclei from the INTEGRAL survey. *Astronomy Letters*, 38(8):475–491.

Koss, M., Trakhtenbrot, B., Ricci, C., Lamperti, I., Oh, K., Berney, S., Schawinski, K., Baloković, M., Baronchelli, L., Crenshaw, D. M., Fischer, T., Gehrels, N., Harrison, F., Hashimoto, Y., Hogg, D., Ichikawa, K., Masetti, N., Mushotzky, R., Sartori, L., Stern, D., Treister, E., Ueda, Y., Veilleux, S., and Winter, L. (2017). BAT AGN Spectroscopic Survey. I. Spectral Measurements, Derived Quantities, and AGN Demographics. *ApJ* , 850(1):74.

Krongold, Y., Dultzin-Hacyan, D., and Marziani, P. (2002). The Circumgalactic Environment of Bright IRAS Galaxies. *ApJ* , 572(1):169–177.

Lacerda, E. A. D., Sánchez, S. F., Cid Fernandes, R., López-Cobá, C., Espinosa-Ponce, C., and Galbany, L. (2020). Galaxies hosting an active galactic nucleus: a view from the CALIFA survey. *MNRAS* , 492(3):3073–3090.

Laor, A. (2001). On the Linearity of the Black Hole-Bulge Mass Relation in Active and in Nearby Galaxies. *ApJ* , 553(2):677–682.

Laor, A. (2003). On the Nature of Low-Luminosity Narrow-Line Active Galactic Nuclei. *ApJ* , 590(1):86–94.

Leahy, D. A. and Creighton, J. (1993). Montecarlo Simulations of X-Ray Spectra for Internally Illuminated Spherical Matter Distributions. *MNRAS* , 263:314.

López-Cobá, C., Sánchez, S. F., Bland-Hawthorn, J., Moiseev, A. V., Cruz-González, I., García-Benito, R., Barrera-Ballesteros, J. K., and Galbany, L. (2019). Systematic study of outflows in the Local Universe using CALIFA: I. Sample selection and main properties. *MNRAS* , 482(3):4032–4056.

Marchesi, S., Ajello, M., Marcotulli, L., Comastri, A., Lanzuisi, G., and Vignali, C. (2018). Compton-thick AGNs in the NuSTAR Era. *ApJ* , 854(1):49.

Márquez, I., Masegosa, J., González-Martin, O., Hernández-Garcia, L., Pović, M., Netzer, H., Cazzoli, S., and del Olmo, A. (2017). The AGN nature of LINER nuclear sources. *Frontiers in Astronomy and Space Sciences*, 4:34.

McKernan, B., Ford, K. E. S., and Reynolds, C. S. (2010). Black hole mass, host galaxy classification and AGN activity. *MNRAS* , 407(4):2399–2410.

Nandra, K., O'Neill, P. M., George, I. M., and Reeves, J. N. (2007). An XMM-Newton survey of broad iron lines in Seyfert galaxies. *MNRAS* , 382(1):194–228.

Narayan, R. and Yi, I. (1994). Advection-dominated Accretion: A Self-similar Solution. *ApJL* , 428:L13.

Nemmen, R. (2013). Probing The Central Engines Of Low-Luminosity Active Galactic Nuclei. *arXiv e-prints*, page arXiv:1301.7719.

Nenkova, M., Sirocky, M. M., Ivezić, Ž., and Elitzur, M. (2008a). AGN Dusty Tori. I. Handling of Clumpy Media. *ApJ* , 685(1):147–159.

Nenkova, M., Sirocky, M. M., Ivezić, Ž., and Elitzur, M. (2008b). AGN Dusty Tori. I. Handling of Clumpy Media. *ApJ* , 685(1):147–159.

Panagiotou, C. and Walter, R. (2019). Reflection geometries in absorbed and unabsorbed AGN. *A&A* , 626:A40.

Panagiotou, C. and Walter, R. (2020). NuSTAR view of Swift/BAT AGN: The R-Γ correlation. *A&A* , 640:A31.

Ricci, C., Trakhtenbrot, B., Koss, M. J., Ueda, Y., Schawinski, K., Oh, K., Lamperti, I., Mushotzky, R., Treister, E., Ho, L. C., Weigel, A., Bauer, F. E., Paltani, S., Fabian, A. C., Xie, Y., and Gehrels, N. (2017). The close environments of accreting massive black holes are shaped by radiative feedback. *Nature* , 549(7673):488–491.

Ricci, C., Walter, R., Courvoisier, T. J. L., and Paltani, S. (2011). Reflection in Seyfert galaxies and the unified model of AGN. *A&A* , 532:A102.

Sánchez, S. F., Kennicutt, R. C., Gil de Paz, A., van de Ven, G., Vílchez, J. M., Wisotzki, L., Walcher, C. J., Mast, D., Aguerri, J. A. L., Albiol-Pérez, S., Alonso-Herrero, A., Alves, J., Bakos, J., Bartáková, T., Bland-Hawthorn, J., Boselli, A., Bomans, D. J., Castillo-Morales, A., Cortijo-Ferrero, C., de Lorenzo-Cáceres, A., Del Olmo, A., Dettmar, R. J., Díaz, A., Ellis, S., Falcón-Barroso, J., Flores, H., Gallazzi, A., García-Lorenzo, B., González Delgado, R., Gruel, N., Haines, T., Hao, C., Husemann, B., Iglésias-Páramo, J., Jahnke, K., Johnson, B., Jungwiert, B., Kalinova, V., Kehrig, C., Kupko, D., López-Sánchez, Á. R., Lyubenova, M., Marino, R. A., Mármol-Queraltó, E., Márquez, I., Masegosa, J., Meidt, S., Mendez-Abreu, J., Monreal-Ibero, A., Montijo, C., Mourão, A. M., Palacios-Navarro, G., Papaderos, P., Pasquali, A., Peletier, R., Pérez, E., Pérez, I., Quirrenbach, A., Relaño, M., Rosales-Ortega, F. F., Roth, M. M., Ruiz-Lara, T., Sánchez-Blázquez, P., Sengupta, C., Singh, R., Stanishev, V., Trager, S. C., Vazdekis, A., Viironen, K., Wild, V., Zibetti, S., and Ziegler, B. (2012). CALIFA, the Calar Alto Legacy Integral Field Area survey. I. Survey presentation. *A&A* , 538:A8.

Shakura, N. I. and Sunyaev, R. A. (1973). Reprint of 1973A&A....24..337S. Black holes in binary systems. Observational appearance. *A&A* , 500:33–51.

Stasińska, G., Vale Asari, N., Cid Fernandes, R., Gomes, J. M., Schlickmann, M., Mateus, A., Schoenell, W., Sodré, L., J., and Seagal Collaboration (2008). Can retired galaxies mimic active galaxies? Clues from the Sloan Digital Sky Survey. *MNRAS* , 391(1):L29–L33.

Urry, C. M. and Padovani, P. (1995). Unified Schemes for Radio-Loud Active Galactic Nuclei. *PASP* , 107:803.

van den Bosch, R. C. E. (2016). Unification of the fundamental plane and Super Massive Black Hole Masses. *ApJ* , 831(2):134.

van den Bosch, R. C. E., Gebhardt, K., Gültekin, K., Yıldırım, A., and Walsh, J. L. (2015). Hunting for Supermassive Black Holes in Nearby Galaxies With the Hobby-Eberly Telescope. *ApJS* , 218(1):10.

Vasudevan, R. V. and Fabian, A. C. (2009). Simultaneous X-ray/optical/UV snapshots of active galactic nuclei from XMM-Newton: spectral energy distributions for the reverberation mapped sample. *MNRAS* , 392(3):1124–1140.

Woo, J.-H. and Urry, C. M. (2002). Active Galactic Nucleus Black Hole Masses and Bolometric Luminosities. *ApJ* , 579(2):530–544.

Yan, R., Ho, L. C., Newman, J. A., Coil, A. L., Willmer, C. N. A., Laird, E. S., Georgakakis, A., Aird, J., Barmby, P., Bundy, K., Cooper, M. C., Davis, M., Faber, S. M., Fang, T., Griffith, R. L., Koekemoer, A. M., Koo, D. C., Nandra, K., Park, S. Q., Sarajedini, V. L., Weiner, B. J., and Willner, S. P. (2011). AEGIS: Demographics of X-ray and Optically Selected Active Galactic Nuclei. *ApJ* , 728(1):38.

Zackrisson, E. (2005). *Quasars and Low Surface Brightness Galaxies as Probes of Dark Matter.* PhD thesis, Department of Astronomy and Space Physics, Uppsala University, Sweden.

Appendix

A1. Sample for the torus evolution analysis

Name (1)	Other name (2)	ra deg (3)	dec deg (4)	Redshift (5)	Dist. Mpc (6)	log M_{BH} (7)	AGN type (8)	Galaxy type (9)	Obs. date (10)	Obs ID (11)	Exp. time ks (12)	Ext. radius arcmin (13)
NGC1052	PKS0238-084	40.26999	-8.25576	0.0048	20.6	8.4	L2	E4	2017-01-17	60201056002	59.75	0.5
NGC2655	ARP225	133.90721	78.22308	0.0057	24.4	8.0	L2	Sa-0	2016-11-10	60160341004	15.95	2
UGC5101	CGCG289-011	143.96539	61.35292	0.0394	168.6	8.3	L1	S?	2014-03-21	60001068002	18.29	1
M81	NGC3031	148.88822	69.06530	0.0009	3.7	7.8	L1.8	SAab	2015-05-18	60101049002	209.09	0.5
NGC3079	UGC05387	150.49085	55.67979	0.0038	16.4	7.2	L2	SBc	2013-11-12	60061097002	21.54	0.5
UGC5881	CGCG125-008	161.67715	25.93155	0.0206	88.2	8.2	L2	Sa	2015-05-17	60160409002	21.41	1
NGC3628	UGC06350	170.07091	13.58949	0.0023	9.8	7.2	L2	SAb	2017-12-23	60371004002	50.35	1
NGC3718	ARP214	173.14522	53.06791	0.0034	14.7	8.3	L1	SB	2017-10-27	60301031004	90.37	0.5
NGC3998	UGC06946	179.48389	55.45359	0.0047	20.1	9.0	L1.9	Sa-0	2016-10-25	60201050002	103.94	0.5
NGC4102	UGC07096	181.59631	52.71095	0.0046	19.5	8.2	L2	SAB	2015-11-19	60160472002	20.57	0.5
M106	NGC4258	184.74008	47.30372	0.0017	7.3	7.5	L1.9	SBbc	2016-01-10	60101046004	103.62	0.5
M58	NGC4579	189.43165	11.81809	0.0043	18.4	7.9	L1.9	Sb	2016-12-06	60201051002	117.84	0.5
NGC5005	UGC08256	197.73463	37.05894	0.0047	20.1	8.1	L1.9	SABb	2014-12-16	60001162002	49.70	1
NGC6240	IC4625	253.24525	2.40099	0.0245	104.8	9.1	L2	S0-a	2014-03-30	60002040002	30.86	0.5
MCG+08-31-041	ARP102B	259.81038	48.98040	0.0242	103.5	8.9	L1	E0	2015-11-24	60160662002	22.40	1
NGC7130	IC5135	327.08121	-34.95131	0.0162	69.2	7.5	L2	Sa	2016-12-15	60261006002	42.12	0.5
NGC7331	UGC12113	339.26709	34.41592	0.0031	13.4	7.8	L2	Sbc	2016-05-03	40202013002	42.97	1
NGC7479	UGC12343	346.23612	12.32288	0.0066	28.3	7.3	L1.9	SBbc	2016-05-12	60201037002	18.45	1
NGC253	ESO474-G029	11.88806	-25.28880	0.0008	3.2	6.9	S2	SAB	2012-09-15	50002031004	157.65	0.5
NGC424	ESO296-G004	17.86516	-38.08345	0.0118	50.7	7.5	S1	SB0-a	2013-01-26	60061007002	15.48	1
IC1657	ESO352-G024	18.52924	-32.65090	0.0107	45.9	7.3	S2	SBbc	2017-01-15	60261007002	45.16	0.5
2MXJ0114-5523	NGC0454NED0	18.60388	-55.39705	0.0121	51.9	8.5	S2	II	2016-02-14	60061009002	24.23	1
MCG+08-03-018	2MXJ0122+5003	20.64341	50.05496	0.0204	87.4	8.4	S2	S?	2014-01-27	60061010002	31.66	1
NGC612	ESO353-G015	23.49063	-36.49328	0.0298	127.5	8.5	S2	SA0	2012-09-14	60061014002	16.69	0.5
Mrk573	UGC01214	25.99074	2.34987	0.0172	73.6	7.4	S2	S0	2018-01-06	60360004002	32.00	1
NGC788	MCG-01-06-025	30.27693	-6.81587	0.0136	58.3	7.7	S2	S0-a	2013-01-28	60061018002	15.41	0.5
M77	NGC1068	40.66988	-0.01329	0.0025	10.6	7.2	S2	SAb	2012-12-18	60002030002	57.85	0.5
NGC1106	UGC02322	42.66873	41.67158	0.0145	62.0	7.5	S2	SA0	2019-02-22	60469002002	18.74	1
NGC1125	MCG-03-08-035	42.91792	-16.65111	0.0109	46.8	7.2	S2	SAB0	2019-06-10	60510001002	31.74	1
NGC1142	UGC02389	43.80095	-0.18355	0.0288	123.5	8.9	S2	Spec	2017-10-14	60368001002	20.71	0.5
Mrk1066	UGC02456	44.99415	36.82050	0.0121	51.7	7.0	S2	SB0	2014-12-06	60001154002	30.08	1
NGC1194	UGC02514	45.95463	-1.10375	0.0136	58.2	7.8	S1.9	SA0	2015-02-28	60061035002	31.54	0.5
NGC1229	ESO480-G033	47.04513	-22.96025	0.0363	155.4	8.3	S2	SBb	2013-07-05	60061325002	24.92	1
NGC1320	MRK0607	51.20288	-3.04226	0.0088	37.7	6.9	S2	Sa	2013-02-10	60061036004	28.00	1
NGC1358	MCG-01-10-003	53.41535	-5.08951	0.0134	57.5	8.1	S2	SAB0	2017-08-01	60301026002	50.00	0.5
NGC1386	ESO358-G035	54.19266	-35.99927	0.0038	16.1	7.0	S1	S0-a	2016-05-11	60201024002	26.43	1
UGC3157	CGCG468-001	71.62399	18.46091	0.0154	66.0	8.0	S2	SBbc	2014-03-18	60061051002	20.09	1
2MJ0508+1721	CGCG468-002NED01	77.08211	17.36336	0.0175	75.0	8.6	S2	-	2012-07-23	60006011002	15.52	0.5
ESO5-4	IRAS06220-8636	91.42384	-86.63195	0.0060	25.9	7.6	S2	Sb	2015-11-10	60061063002	24.70	1
NGC2273	UGC03546	102.53614	60.84580	0.0068	29.0	7.0	S2	SBa	2014-03-23	60001064002	23.23	1
UGC3601	CGCG204-032	103.95638	40.00031	0.0171	73.3	8.6	S1.5	S?	2019-01-06	60160278002	19.67	1
ESO428-14	MCG-05-18-002	109.13003	-29.32469	0.0054	23.2	7.0	S2	SA0	2015-01-11	60001152002	40.25	0.5
2MXJ0756-4137	WAJ075619.61-413742.1	119.08182	-41.62835	0.0210	90.1	8.0	S2	-	2014-07-29	60061076002	22.75	2
NGC2788A	ESO060-G024	135.66418	-68.22683	0.0144	61.6	8.7	S2	Sb	2019-06-14	60469001002	27.58	0.5
IC2560	ESO375-G004	154.07795	-33.56381	0.0078	33.4	7.2	S2	SBbc	2014-07-16	50001039004	49.56	1
NGC3147	UGC05532	154.22347	73.40065	0.0092	39.6	8.7	S2	SAbc	2015-12-27	60101032002	49.26	0.5
NGC3393	ESO501-G100	162.09778	-25.16203	0.0125	53.6	7.5	S2	SBab	2013-01-28	60061205002	15.66	0.5
2MXJ1105+5856	CGCG291-028	166.49593	58.94603	0.0271	116.0	8.4	S2	-	2019-03-26	60160420002	15.77	2
NGC3621	ESO377-G037	169.56792	-32.81260	0.0016	6.7	6.8	S2	SA	2017-12-15	60371002002	30.78	2
NGC3786	UGC06621	174.92714	31.90943	0.0118	50.6	7.5	S1.8	SAB	2014-06-09	60061349002	21.99	2
NGC3982	UGC06918	179.11737	55.12536	0.0052	22.1	6.3	S2	SABb	2017-12-06	60375001002	33.41	1
IC751	UGC06972	179.71915	42.57034	0.0312	133.6	8.6	S2	Sb	2013-02-04	60061217004	52.02	0.5
M88	NGC4501	187.99673	14.42041	0.0042	18.0	7.5	S2	SAb	2018-01-26	60375002002	62.77	1
IC3639	ESO381-G008	190.22015	-36.75585	0.0109	46.8	6.9	S2	SBbc	2015-01-09	60001164002	58.73	0.5
NGC4785	ESO219-G004	193.36382	-48.74915	0.0116	49.6	8.1	S2	SAB	2014-08-20	60001143002	48.83	0.5
Mrk231	UGC08058	194.05931	56.87368	0.0422	180.6	8.4	S2	Sc	2017-10-19	80302608002	82.06	0.5
NGC4941	PGC045165	196.05461	-5.55160	0.0033	14.2	6.9	S2	SABa	2016-01-19	60061236002	20.66	1
NGC4939	MCG-02-33-104	196.05970	-10.33953	0.0085	36.4	7.9	S2	Sbc	2017-02-17	60002036002	22.04	0.5
NGC4945	ESO219-G024	196.36366	-49.46790	0.0010	4.2	6.3	S2	SBc	2013-06-15	60002051004	54.62	0.5
MCG-03-34-064	PGC046710	200.60202	-16.72836	0.0200	85.6	8.1	S1.8	SB?	2016-01-17	60101020002	78.50	0.5
NGC5135	ESO444-G032	201.43358	-29.83368	0.0015	6.3	7.6	S2	Sab	2015-01-14	60001153002	33.36	1
M51a	NGC5194	202.46957	47.19526	0.0017	7.3	6.6	S2	-	2017-03-17	60201062003	163.06	0.5
NGC5252	UGC08622	204.56613	4.54265	0.0195	83.6	8.9	S1.9	S0	2013-05-11	60061245002	19.01	0.5
NGC5283	UGC08672	205.27395	67.67222	0.0106	45.3	7.7	S2	S0	2018-11-17	60465006002	33.02	0.5
NGC5347	UGC08805	208.32416	33.49083	0.0050	21.6	6.8	S2	Sab	2015-01-16	60001163002	47.30	1
NGC5643	ESO272-G016	218.16991	-44.17461	0.0027	11.4	7.0	S2	Sc	2014-05-24	60061362002	22.46	1
NGC5695	UGC09421	219.34223	36.56783	0.0125	53.5	7.7	S2	SBb	2018-01-16	60368004002	41.61	1
NGC5728	MCG-03-37-005	220.59970	-17.25317	0.0071	30.3	7.8	S2	SABa	2013-01-02	60061256002	24.36	0.5
NGC5899	UGC09789	228.76355	42.04985	0.0090	38.6	8.7	S2	SABc	2014-04-08	60061348002	23.88	0.5
MCG+14-08-004	CGCG367-009	244.83058	81.04650	0.0239	102.4	9.8	S2	-	2014-12-21	60061270002	29.76	1
ESO137-34	2MXJ1635-5804	248.80881	-58.08003	0.0077	33.0	8.0	S2	SAB0	2016-06-07	60061272002	18.55	0.5
2MXJ1650+0436	NGC6230NED01	252.67813	4.60508	0.0321	137.3	9.8	S2	-	2017-02-06	60061273002	21.03	0.5
2MXIJ1802-1454	WAJ180247.38-145454.8	270.69708	-14.91528	0.0034	14.6	7.8	S1	-	2016-05-01	60160680002	19.96	0.5
2MXJ18305+0928	LEDA1365707	277.71098	9.47830	0.0194	83.2	8.4	S2	-	2015-11-15	60061285002	22.72	1
IC4995	ESO186-G034	304.99574	-52.62192	0.0161	68.9	7.2	S2	SA0	2019-06-03	60360003002	34.00	1
NGC6921	UGC11570	307.12018	25.72339	0.0145	62.0	8.4	S2	SA0	2013-05-18	60061300002	19.52	1
NGC7213	ESO288-G043	332.31754	-47.16669	0.0051	22.0	7.7	S1.5	Sa	2014-10-05	60001031002	101.62	0.5
NGC7319	UGC12102	339.01501	33.97588	0.0109	46.7	7.3	S2	SBbc	2017-09-27	60261005002	41.88	0.5
UGC12282	CGCG532-004	344.73035	40.93221	0.0169	72.4	9.8	S1.9	Sa	2019-11-18	60160812002	28.56	1
NGC7582	ESO291-G016	349.59842	-42.37057	0.0049	21.2	7.6	S1.5	SBab	2016-04-28	60201003002	48.49	0.5
2MXJ2325-3826	IRAS23226-3843	351.35078	-38.44700	0.0359	153.8	8.2	S1	-	2017-06-11	80101001002	96.61	0.5
NGC7674	UGC12608	351.98624	8.77895	0.0174	74.5	7.6	S2	SAbc	2014-09-30	60001151002	52.00	0.5

Table 3: Observational parameters for the torus evolution sample. (1) Name of the source; (2) other name (3) right ascension; (4) declination; (5) Redshift; (6) Distance in Mpc; (7) Galaxy type. All galaxy types were retrieved from NED; (8) AGN classification; (9) Black hole mass; (10) date of the observation; (11) Observation ID in *NuSTAR*; (12) Exposure time of the observation in ksec; (13) is the extraction radius used in the data reduction. In columns (1) and (2), 2MXJ (2MXIJ) is abbreviation for 2MASXJ (2MASXIJ), 2M is the abbreviation for 2MASS and W is the abbreviation for WISE.

A2. Sample for the CALIFA analysis

Name	RA deg	DEC deg	D Mpc	z	Obsid	Exptime ks	Outer rad. arcsec	Name	RA deg	DEC deg	D Mpc	z	Obsid	Exptime ks	Outer rad. arcsec
(1)	(2)	(3)	(4)	(5)	(6)	(7)	(8)	(9)	(10)	(11)	(12)	(13)	(14) (15)	(16)	
NGC7803	0.33	13.11	76.7	0.0177	6978	28.17	-	NGC3896	177.23	48.67	13.1	0.0032	21091	10.07	-
NGC0023	2.47	25.92	51.5	0.0157	10401	19.98	13	NGC3945	178.31	60.68	23.2	0.0043	6780	15.17	-
NGC0192	9.81	0.86	59.0	0.0139	8171	19.42	-	NGC4059	181.05	20.41	107.2	0.0238	12990	5.06	-
NGC0197	9.83	0.89	58.9	0.0108	8171	19.42	-	IC3065	183.80	14.43	17.1	0.0033	8076	5.17	-
NGC0214	10.37	25.50	51.1	0.0151	9098	5.04	-	NGC4291	185.07	75.37	35.4	0.0058	11778	30.16	16
NGC0384	16.85	32.29	60.7	0.0140	2147	44.98	-	NGC4390	186.46	10.46	22.4	0.0037	19425	15.56	-
NGC0495	20.73	33.47	69.9	0.0135	10536	18.64	-	PGC040616	186.49	10.05	17.0	0.0034	8128	5.16	-
NGC0499	20.80	33.46	66.8	0.0147	10536	18.64	18	NGC4470	187.41	7.82	18.8	0.0081	12888	161.35	16
NGC0496	20.80	33.53	63.4	0.0201	10536	18.64	-	NGC4479	187.58	13.58	18.3	0.0029	8066	5.16	-
NGC0504	20.87	33.20	64.7	0.0140	317	27.19	-	NGC4486B	187.63	12.49	15.4	0.0053	5827	158.27	6
NGC0507	20.92	33.26	69.1	0.0164	317	27.19	13	IC3586	189.23	12.52	20.0	0.0057	8083	5.16	-
NGC0508	20.92	33.28	76.7	0.0184	317	27.19	-	IC3652	190.24	11.18	15.2	0.0019	8079	5.16	-
NGC0548	21.51	-1.23	82.0	0.0180	7823	65.68	-	NGC4676A	191.54	30.73	94.5	0.0222	2043	28.91	-
NGC0741	29.09	5.63	70.7	0.0184	17198	92.62	16	NGC4676B	191.55	30.72	94.4	0.0216	2043	28.91	-
MCG-02-06-016	30.23	-8.84	23.0	0.0059	6106	35.77	-	PGC092948	191.60	11.95	186.3	0.0461	8101	5.16	-
NGC0833	32.34	-10.13	55.2	0.0127	15667	59.11	-	NGC4841A	194.38	28.48	90.5	0.0226	20052	24.05	-
NGC0835	32.35	-10.14	34.0	0.0133	15667	59.11	11	NGC4861	194.75	34.84	7.5	0.0015	20992	59.23	13
PGC008502	33.32	-7.66	68.4	0.0010	18022	30.06	-	NGC4874	194.90	27.96	96.9	0.0240	13996	124.68	14
NGC0890	35.50	33.27	37.0	0.0131	19325	35.06	-	NGC5198	202.55	46.67	48.5	0.0084	6786	14.97	28
UGC01859	36.18	42.62	116.0	0.0198	17064	10.04	-	NGC5216	203.03	62.70	62.1	0.0099	10568	5.47	-
IC0225	36.62	1.16	18.6	0.0052	11351	7.56	-	NGC5218	203.04	62.77	51.4	0.0097	10568	5.47	-
NGC0991	38.89	-7.15	8.8	0.0052	7861	5.11	-	NGC5358	208.50	40.28	34.5	0.0081	14903	40.8	-
NGC1060	40.81	32.42	78.4	0.0172	18713	29.57	21	NGC5394	209.64	37.45	32.9	0.0117	10395	16.08	-
NGC1132	43.22	-1.28	87.9	0.0232	3576	40.17	15	NGC5395	209.66	37.42	46.4	0.0116	10395	16.08	-
NGC1129	43.61	41.58	74.2	0.0177	908	48.46	16	NGC5426	210.85	-6.07	34.1	0.0086	4847	9.74	30
PGC11179	44.39	5.98	110.5	0.0227	4181	21.78	-	NGC5427	210.86	-6.03	33.8	0.0091	4847	9.74	-
NGC1167	45.43	35.21	70.6	0.0165	19313	13.05	-	NGC5473	211.18	54.89	27.3	0.0067	19322	9.95	-
NGC1259	49.32	41.38	71.7	0.0194	9097	35.18	-	NGC5485	211.80	55.00	29.8	0.0064	19375	10.07	-
NGC1270	49.74	41.47	80.8	0.0163	502	5.38	12	NGC5532	214.22	10.81	69.5	0.0248	3968	50.08	13
NGC1271	49.80	41.35	82.2	0.0199	12037	85.76	13	NGC5546	214.54	7.56	104.0	0.0246	7057	5.25	-
NGC1277	49.96	41.57	60.7	0.0168	4952	166.42	5	NGC5557	214.61	36.49	38.8	0.0108	19324	8.95	-
NGC1281	50.03	41.63	93.3	0.0141	4952	166.42	15	NGC5576	215.27	3.27	21.0	0.0050	11781	30.05	16
PGC012562	50.25	41.56	68.9	0.0157	4948	120.18	13	NGC5614	216.03	34.86	35.8	0.0129	11679	14.75	-
UGC02698	50.51	40.86	111.1	0.0214	17065	8.07	-	NGC5631	216.64	56.58	24.2	0.0064	19376	10.07	-
NGC2315	105.64	50.59	89.9	0.0204	12564	10.04	-	NGC5623	216.79	33.25	47.9	0.0114	9895	31.03	14
UGC03816	110.80	58.06	61.6	0.0109	16611	32.07	15	NGC5656	217.61	35.32	55.8	0.0107	19673	22.8	-
UGC03995	116.04	29.25	60.6	0.0159	12869	10.96	-	NGC5675	218.17	36.30	56.8	0.0132	9135	36.22	20
NGC2445	116.73	39.01	62.3	0.0133	14906	39.51	-	UGC9562	222.81	35.54	23.8	0.0043	13930	31.04	-
NGC2484	119.62	37.79	171.0	0.0408	858	8.26	-	NGC5794	223.97	49.73	59.6	0.0140	19531	34.6	-
UGC04132	119.80	32.91	75.7	0.0176	7570	33.04	-	NGC5797	224.10	49.70	56.8	0.0134	19531	34.6	-
NGC2513	120.60	9.41	70.3	0.0157	19318	14.06	-	UGC9661	225.51	1.84	17.7	0.0044	12952	144.9	-
NGC2553	124.40	20.90	67.4	0.0155	7935	31.13	-	NGC5845	226.50	1.63	27.1	0.0049	4009	30.79	-
NGC2558	124.80	20.51	81.3	0.0167	7936	28.05	-	NGC5929	231.53	41.67	38.5	0.0084	20623	27.42	30
IC2341	125.92	21.43	74.8	0.0171	7937	30.03	-	NGC5930	231.53	41.68	35.0	0.0087	20623	27.42	-
UGC04414	126.77	21.64	112.0	0.0252	10268	10.15	-	NGC5953	233.63	15.19	27.1	0.0072	2930	10.16	-
NGC2595	126.93	21.48	68.6	0.0143	10268	10.15	-	NGC5954	233.65	15.20	36.4	0.0065	2930	10.16	-
UGC04461	128.34	52.53	69.8	0.0167	1643	9.25	-	ARP220	233.74	23.50	77.6	0.0180	16092	171.46	13
NGC2623	129.60	25.75	81.7	0.0183	4059	20.81	-	NGC6027	239.80	20.76	68.8	0.0148	11261	70.05	-
NGC2639	130.91	50.21	47.7	0.0107	5682	5.08	-	UGC10205	241.67	30.10	122.5	0.0219	20434	7.06	-
NGC2780	138.19	34.93	55.5	0.0067	11777	29.55	-	NGC6090	242.92	52.46	125.5	0.0302	6859	14.98	-
NGC2748	138.43	76.48	19.2	0.0049	11776	30.05	27	NGC6125	244.80	57.98	69.0	0.0158	10550	10.04	-
NGC2787	139.83	69.20	22.3	0.0022	4689	31.24	13	NGC6166NED01	247.16	39.55	132.9	0.0268	498	19.16	19
NGC2805	140.09	64.10	14.0	0.0059	12984	10.06	-	NGC6251	248.13	82.54	98.2	0.0245	4130	49.17	20
NGC2906	143.03	8.44	38.8	0.0072	19298	41.76	22	PGC2172338	249.37	40.88	104.0	0.0263	887	74.32	-
UGC05187	145.78	41.09	20.9	0.0049	19438	49.31	-	NGC6285	254.60	58.96	81.3	0.0189	10566	14.19	-
MCG+08-19-17	154.74	46.45	128.3	0.0297	19033	24.05	-	NGC6286	254.63	58.94	78.6	0.0187	10566	14.19	19
NGC3353	161.34	55.96	18.9	0.0041	13927	18.07	27	NGC6278	255.21	23.01	39.1	0.0093	6789	16.68	-
IC2604	162.35	32.77	23.3	0.0056	2042	19.76	-	NGC6338	258.85	57.41	128.8	0.0275	4194	47.94	23
NGC3395	162.46	32.98	17.6	0.0055	2042	19.76	-	NGC7236	333.69	13.85	91.2	0.0262	6392	33.13	-
NGC3396	162.48	32.99	24.9	0.0059	2042	19.76	-	UGC11958	333.70	13.84	112.6	0.0262	6392	33.13	16
PGC32873	164.07	42.33	106.7	0.0250	21377	58.07	12	UGC12127	339.62	35.33	118.2	0.0276	2191	10.14	20
PGC033423	165.98	40.85	147.9	0.0347	12977	53.01	12	NGC7457	345.25	30.14	13.3	0.0027	17007	45.27	30
NGC3600	168.97	41.59	16.3	0.0025	19356	7.07	-	IC5309	349.80	8.11	53.0	0.0138	2074	27.09	-
NGC3605	169.19	18.02	24.5	0.0020	2073	39.0	-	NGC7611	349.90	8.06	42.6	0.0108	3955	37.95	-
NGC3773	174.55	12.11	17.1	0.0033	17071	10.1	-	NGC7619	350.06	8.21	53.8	0.0126	3955	37.95	18
NGC3842	176.01	19.95	99.6	0.0208	4189	48.11	11	NGC7623	350.13	8.40	51.0	0.0123	2074	27.09	-
NGC3860	176.20	19.79	101.3	0.0187	514	41.05	14	NGC7684	352.63	0.08	73.3	0.0172	8616	8.95	-
NGC3861	176.27	19.97	85.3	0.0169	514	41.05	18	NGC7716	354.13	0.30	32.4	0.0086	11728	17.04	-
NGC3893	177.16	48.71	15.8	0.0033	21091	10.07	-	NGC7052	319.64	26.45	51.5	0.0120	19326	39.06	14

Table 4: Observational parameters for the CALIFA sample. Cols. (1) and (9) are the names of the sources, Cols. (2)-(3) and (10)-(11) are coordinates in degrees, Cols. (4) and (12) are the distance to the sources in Mpc, Cols. (5) and (13) are the redshifts, Cols. (6) and (14) are the *Chandra* observation ID number, Cols. (7) and (15) are the exposure times in kiloseconds, and Cols. (8) and (16) are the extraction radius used in the ring extraction, whenever there was enough SNR to perform the spectral analysis (see text).